

# Development of Advanced Electrochemical Emission Spectroscopy for Monitoring Corrosion in Simulated DOE Liquid Waste

**Digby D. Macdonald (PI), Brian Marx (GS), Balaji Soundararajan (GS), Morgan Smith (GS), Jeng-Kuei Cheng (GS - RoC), Sejin Ahn (GS - Korea), Rajeev Gupta (UGS - India), Julio Ruiz (UGS - Spain).**

**Center for Electrochemical Science and Technology  
Department of Materials Science and Engineering  
Pennsylvania State University  
201 Steidle Bldg  
University Park, PA 16802.**

**Grant No. DE-FG07-01ER62515**

**January 19-21, 2005  
Savannah River National Laboratory**

# OBJECTIVES

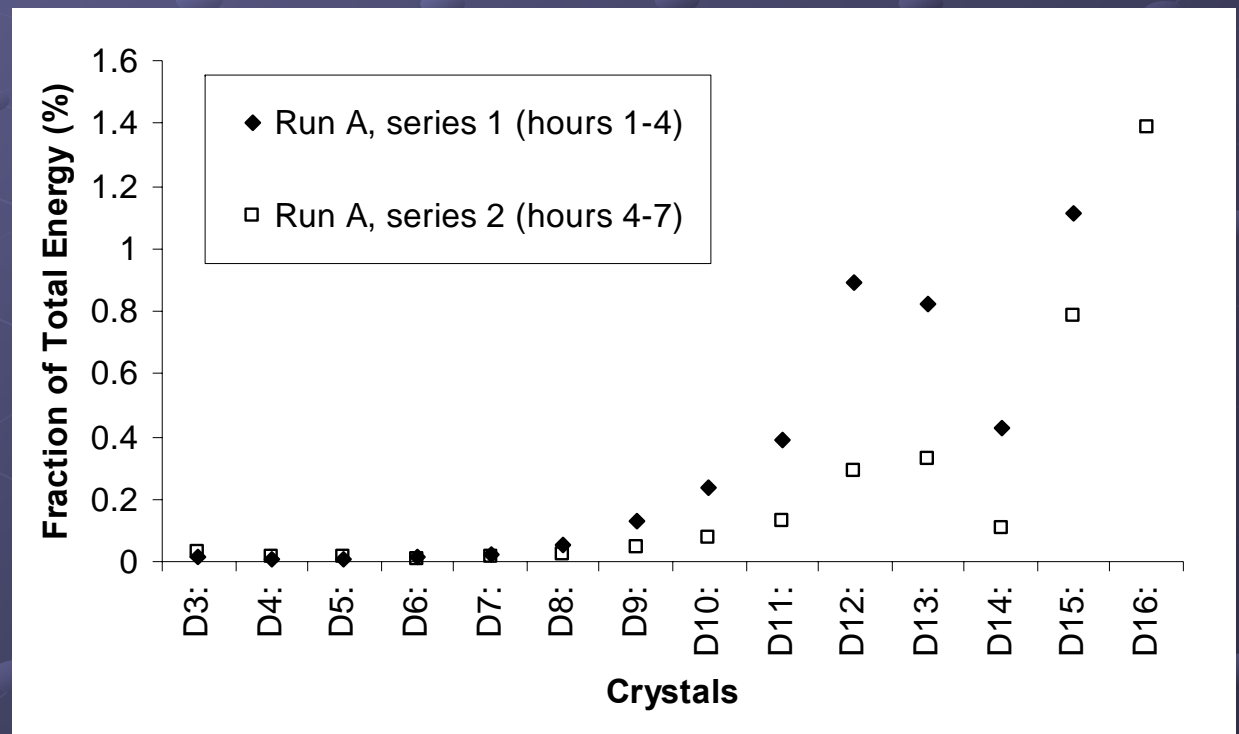
- Develop advanced electrochemical emission spectroscopic techniques for remote *in situ* corrosion monitoring in DOE Liquid Waste storage tanks.
- Explore the mechanisms of the growth and breakdown of protective passive films on iron and carbon steel in aqueous solutions of relevance to liquid waste storage.
- Explore the mechanism(s) of environment-assisted fracture in high strength steel simulating weld heat-affected zones in liquid waste storage tanks.
- Explore the fundamental role of chloride ion in inducing passivity breakdown on metals and alloys.
- Develop deterministic methods for predicting the accumulation of localized corrosion damage to DOE Liquid Waste storage tanks over the corrosion evolutionary path.

# Wavelet Analysis of Electrochemical Noise

- Objective is to not only characterize the severity of corrosion but also to differentiate between general and localized corrosion by remote, in situ monitoring.
- WA is an alternative to FFT and MEMs for transforming data from the time domain to the frequency domain.
- WA has significant advantages over FFT and MEMs, including no need to have the mean of the noise being time invariant.
- Is it an effective method for analyzing electrochemical emission spectroscopic data from DOE Liquid Waste storage tanks?

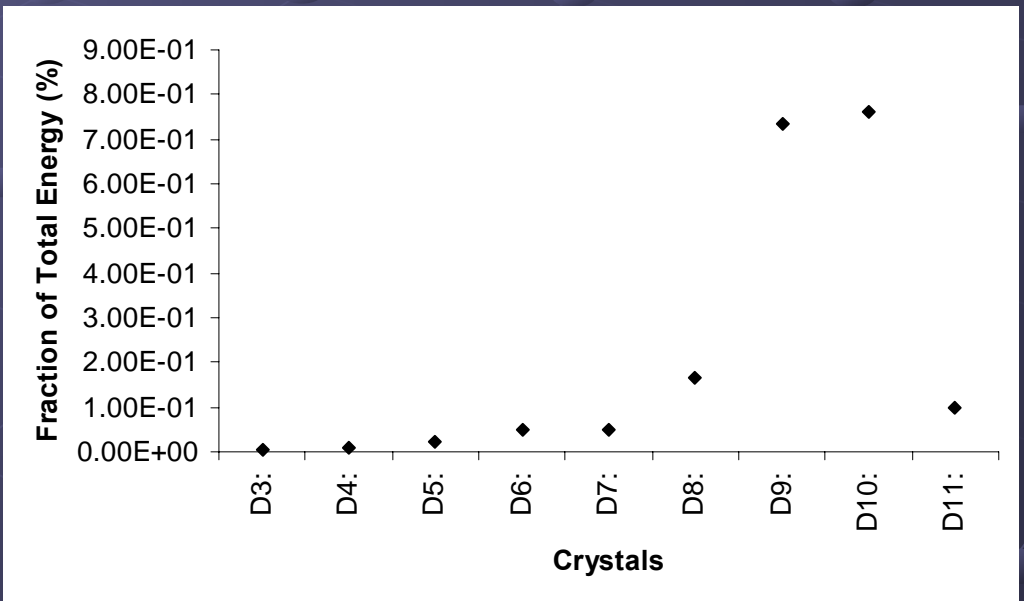
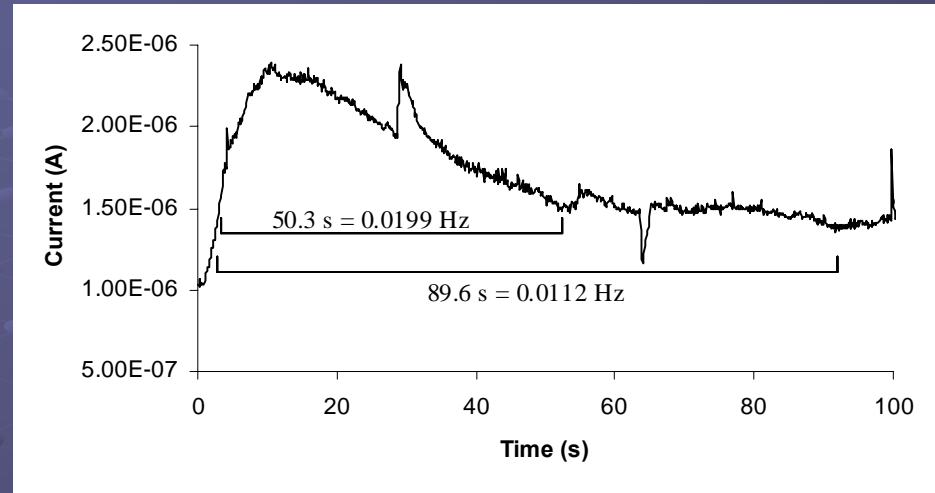
# WA Identification of Pitting

- Results of EDP on current data taken in the first three hours after chloride ion injection (series 1) and the three hours after that (series 2) show WA's ability to identify pitting corrosion.
- Shows pitting corrosion contributes to crystals D9-D13: frequency range 0.00122 – 0.0391 Hz (819.2 s - 25.6 s)
- The second series shows a drop in the energy contribution of crystals D9-D13 which correctly identifies the decrease in pitting corrosion intensity with time.



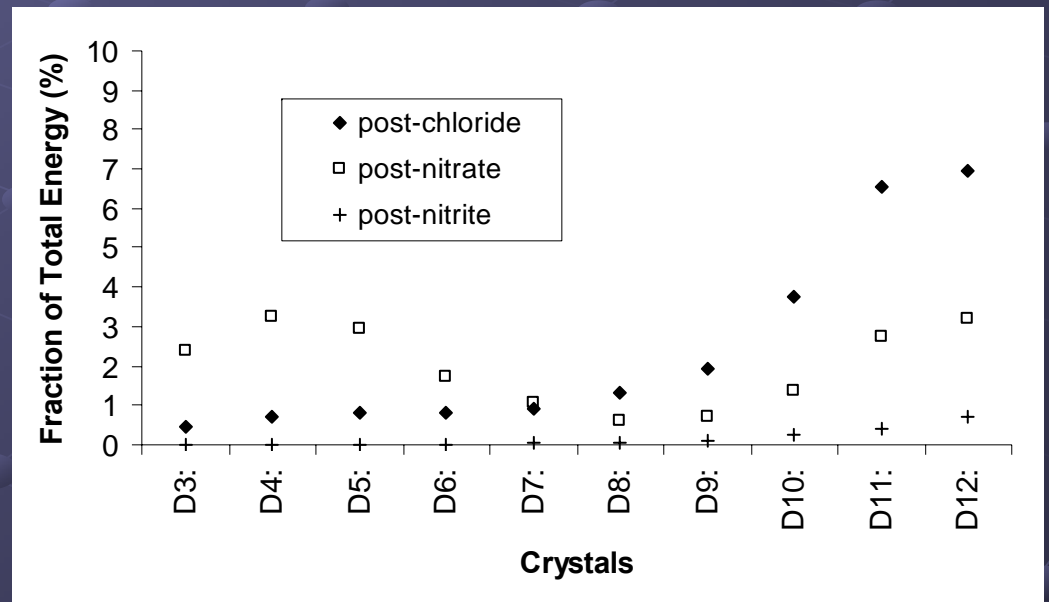
# Confirmation of Pitting Intervals

- Confirmation of the correlation between pitting events and the low-frequency crystals (D8-D11) was achieved by examining a single pitting transient with WA.
- Two repassivation times are shown on the current record. These two times correspond to 0.0199 and 0.0122 Hz or crystals D9 and D10, respectively.
- This is confirmed by the EDP.



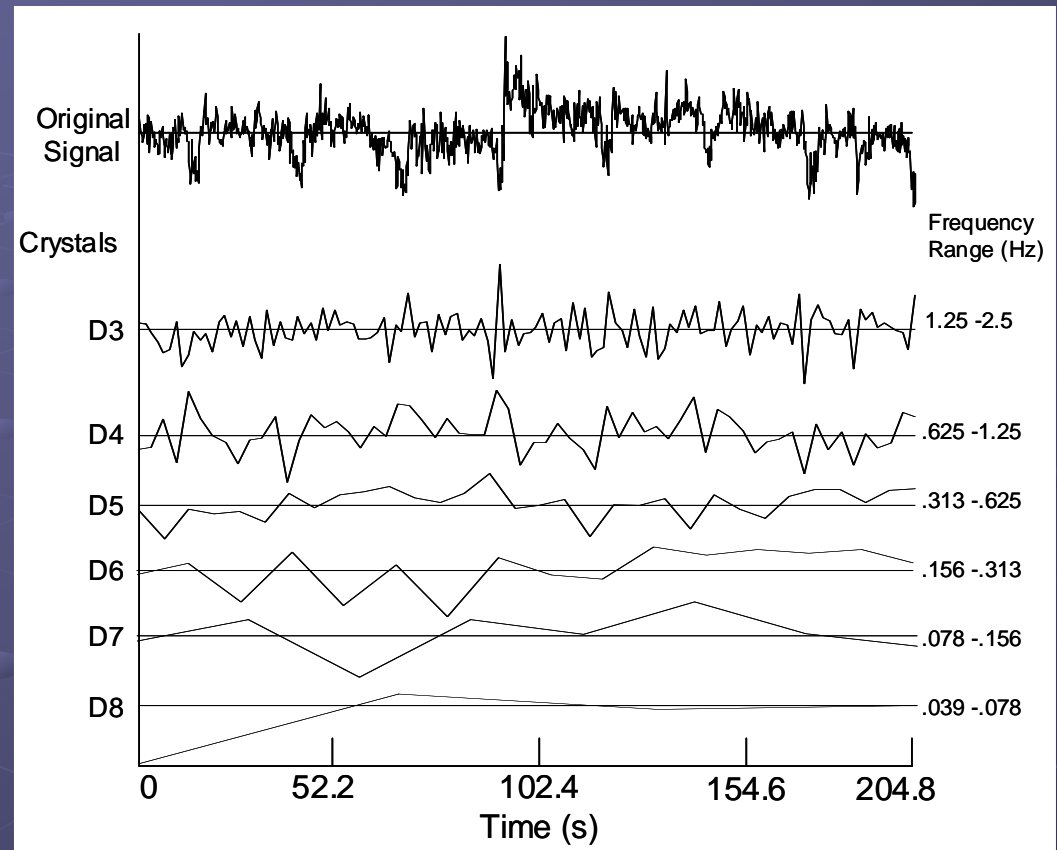
# Chemical Effect Identification

- Chloride ions show contributions to crystals D9-D12 corresponding to pitting corrosion.
- Nitrate injection results show less effective inhibition of corrosion than is seen with nitrite ions, and there is an increase in crystals D3-D6: showing that nitrate ions promote general corrosion in these conditions.
- The injection of nitrite ions effectively inhibited both the general corrosion and the remaining pitting corrosion.



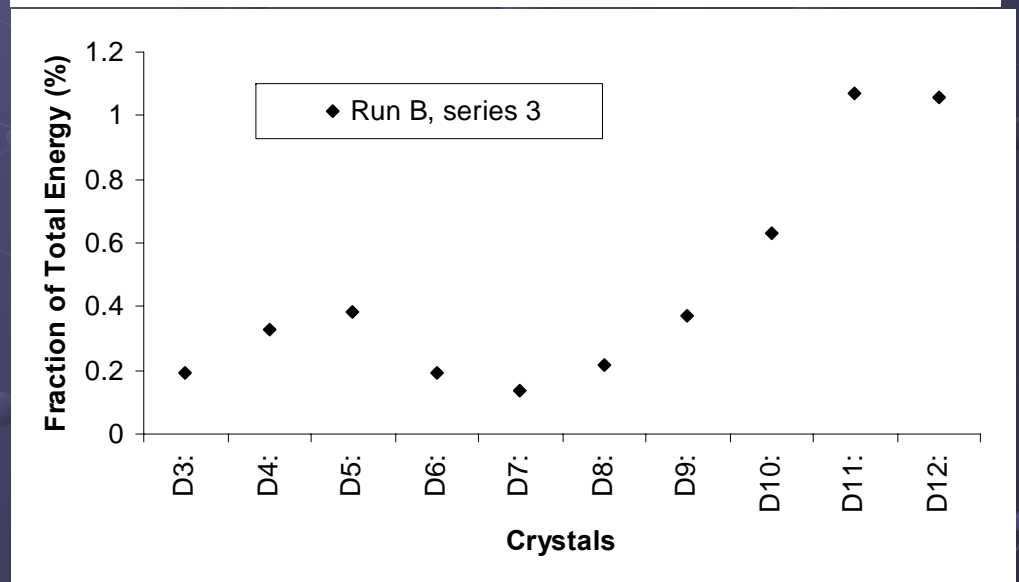
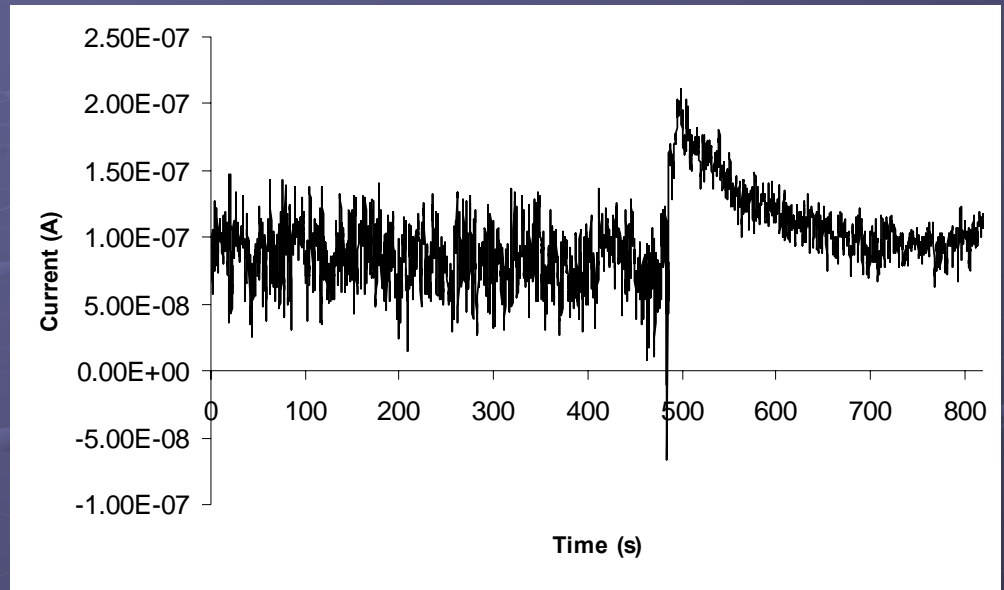
# Time Domain Data Retention

- Unlike many methods currently used on EN, WA retains time domain information.
- This plot of wavelet coefficients from several crystals versus the original current signal shows one possible application.
- The large event at time 98.6 s, has contributions from crystals D3, D4, and D5.
- These contributions can be seen in the peaks in the crystals around time 98.6 s. This shows that events with frequencies from 0.313-2.5 Hz contributed.



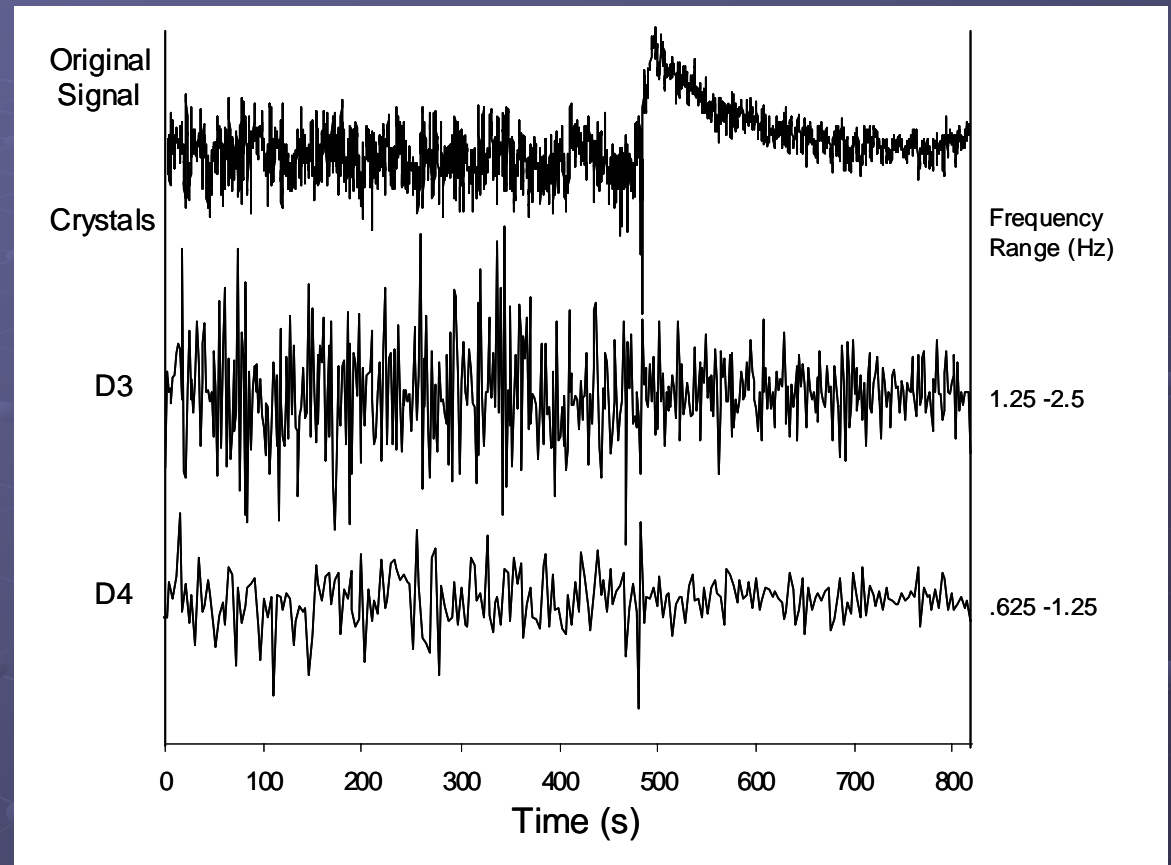
# WA Identifying Multiple Corrosion Types

- Current record before, during, and after the injection of chloride ions shows the random appearance of general corrosion prior to injection, and the repassivation curve of pitting corrosion after.
- EDP of the entire period shows contributions from high- (D3-D6) and low-frequency (D8-D12) crystals, associated with general and pitting corrosion, respectively.



# Corrosion Initiation

- WA can also identify the time of the termination of general corrosion and the initiation of pitting corrosion.
- Here the original signal is compared to the coefficients of high-frequency crystals.
- The magnitudes of the coefficients drop off markedly at the time of injections, a result of those frequencies no longer matching the signal well.
- Calculations of the standard deviations of the coefficients with time indicates the time of corrosion character change.

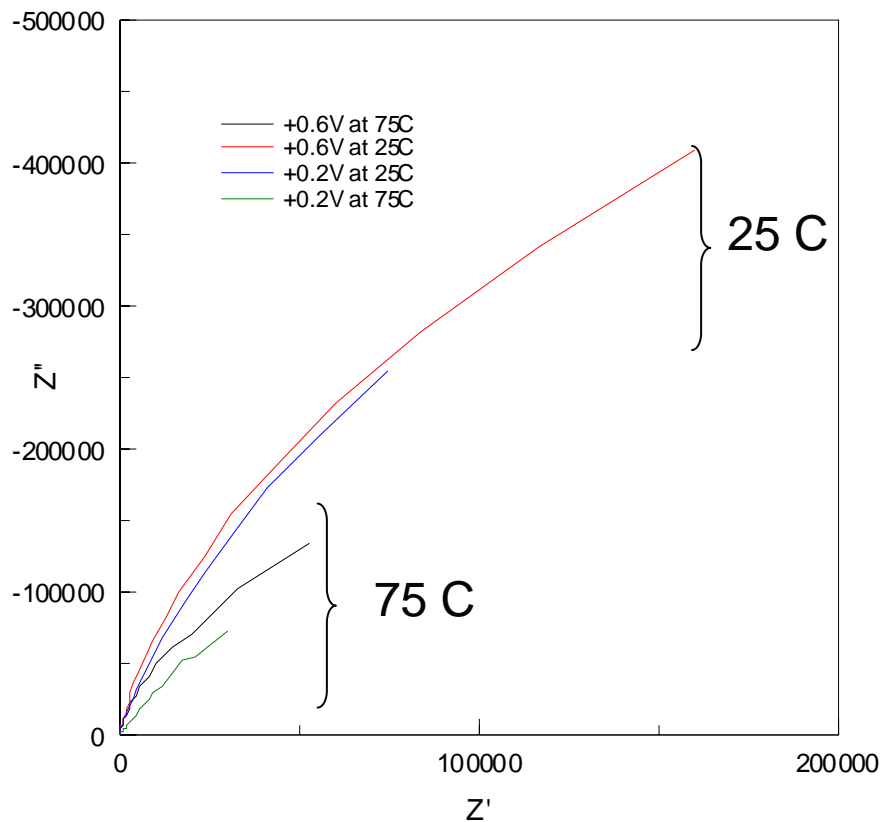


# Mechanism(s) of the Growth and Breakdown of the Passive Film on Iron

- Carbon steel can be used in a Liquid Waste environment only because of the continued existence of a thin oxide film (the “passive” film) on the surface.
- This film is not perfectly protective, because of dissolution at the film/solution interface, transmission of cations through the film, and breakdown by aggressive species, such as chloride ion.
- Growth and breakdown of the film is well accounted for by the Point Defect Model (PDM, see previous workshops).
- Emphasis in the present work has been on the generation of values for various PDM parameters and the application of Damage Function Analysis (DFA) to the prediction of localized (pitting) corrosion to the storage tanks in the field (just begun).

# Impedance of Iron with Temp

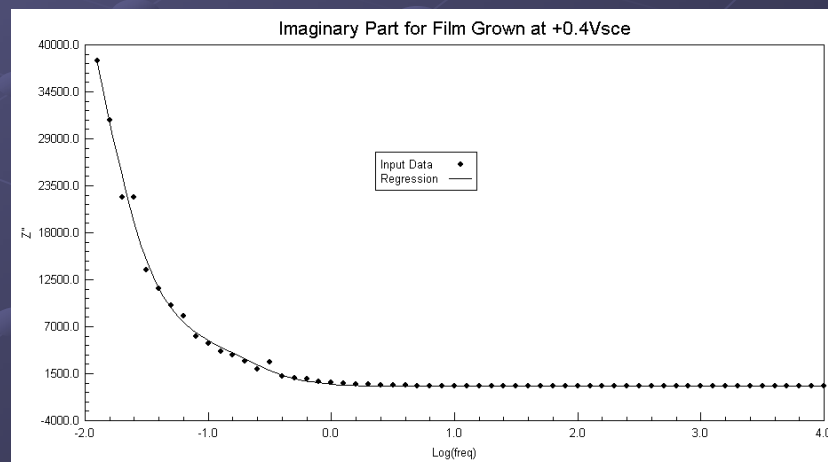
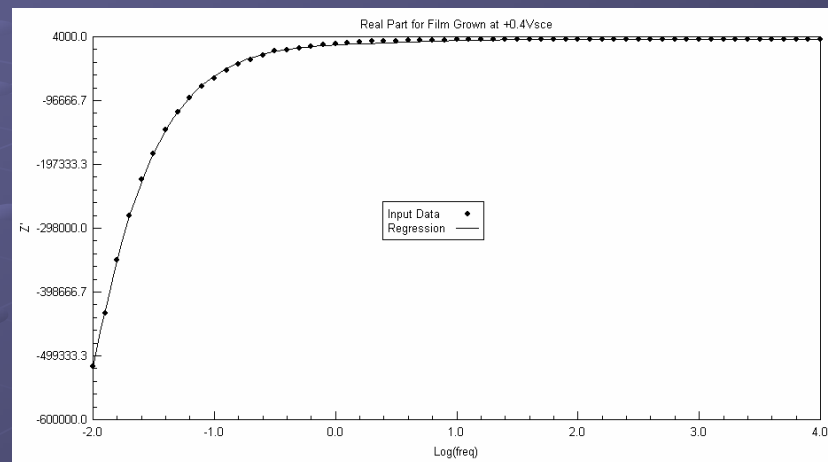
## Impedance for Steady-State Films



This is a plot showing the impedance for a film grown on iron in borate buffer solution containing EDTA at a pH of 8.15. The impedance greatly diminishes with temp. The impedance for films grown at 0.2  $V_{SCE}$  (near lower end of passive region) and 0.6  $V_{SCE}$  (near upper end of passive region) are shown here to make it easier to view.

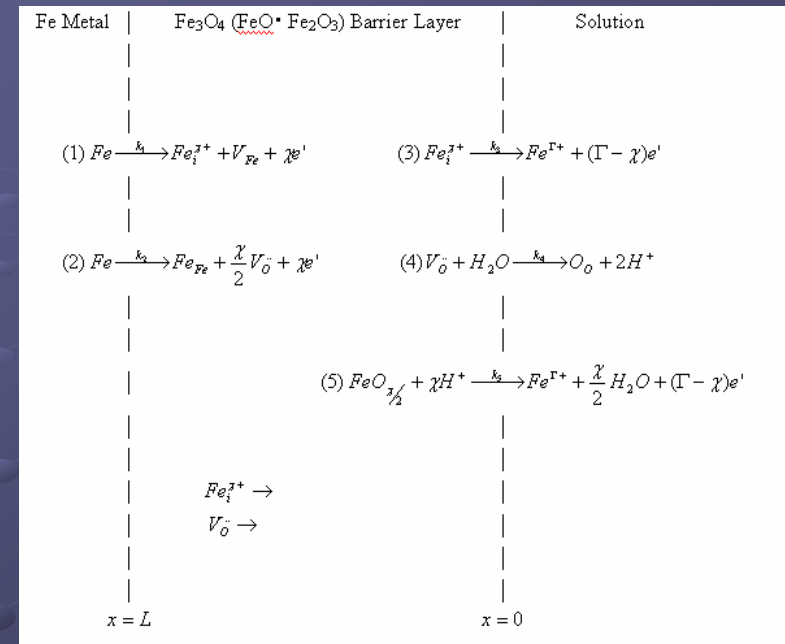
# Fitting Equation to Data to Extract the PDM Parameters

- **Figure 1.** Real part (a) and imaginary part (b) of impedance data for the passive film formed on iron in borate buffer solution with 0.01 M EDTA (pH 8.15) at an applied film formation voltage of 0.4 V vs. SCE, plotted as a function of experimental frequencies ranging from .01Hz to 10000 Hz.
- The admittance equation is separated into the real and imaginary parts of the impedance and then fitted to the data to yield the unknown parameters in the model.
- Note: Fitting to both the real and imaginary parts is a method of self-checking.



# Fundamental Parameters

Parameter	Room Temp.	75C
$\alpha_1$	0.01 (from regression)	0.0007 (from regression)
$\alpha_2$	0.24 (from regression)	0.06 (from regression)
$\alpha_3$	0.39 (from regression)	0.45 (from regression)
$\alpha_5$	0.30 (from regression)	0.12 (from regression)
$k_1^{00} (mol \cdot cm^{-2} \cdot s^{-1})$	$3.8 \times 10^{-12}$ (from regression)	$9.9 \times 10^{-10}$ (from regression)
$k_2^{00} (mol \cdot cm^{-2} \cdot s^{-1})$	$1.1 \times 10^{-15}$ (from regression)	$1.8 \times 10^{-20}$ (from regression)
$k_3^{00} (s^{-1})$	$2.4 \times 10^{-6}$ (from regression)	$3.85 \times 10^{-7}$ (from regression)
$k_5^{00} (mol^{0.4} \cdot cm^{-0.2} \cdot s^{-1})$	$3.3 \times 10^{-8}$ (from regression)	$4.61 \times 10^{-8}$ (from regression)
$\beta$	-0.0047 (from regression)	.0002 (from regression)
$\phi_{f/s}^0 (V \text{ vs. } SCE)$	-0.29 (from regression)	-.007 (from regression)
$\hat{\epsilon}$	30 (from Reference [3])	30 (from Reference [3])
$\epsilon (V/cm)$	$1.10 \times 10^6$ (from Reference [12])	$1.10 \times 10^6$ (from Reference [12])
$\alpha$	0.728 (from Reference [12])	0.728 (from Reference [12])



$\alpha_i$ =transfer coefficient for ith reaction

$k_i^{00}$ = standard rate constant for ith reaction

$\beta$ =dependence of potential drop at f/s on pH

$\alpha$ =dependence of potential drop at f/s on V

$\epsilon$ =electric field strength within film (assumed constant)

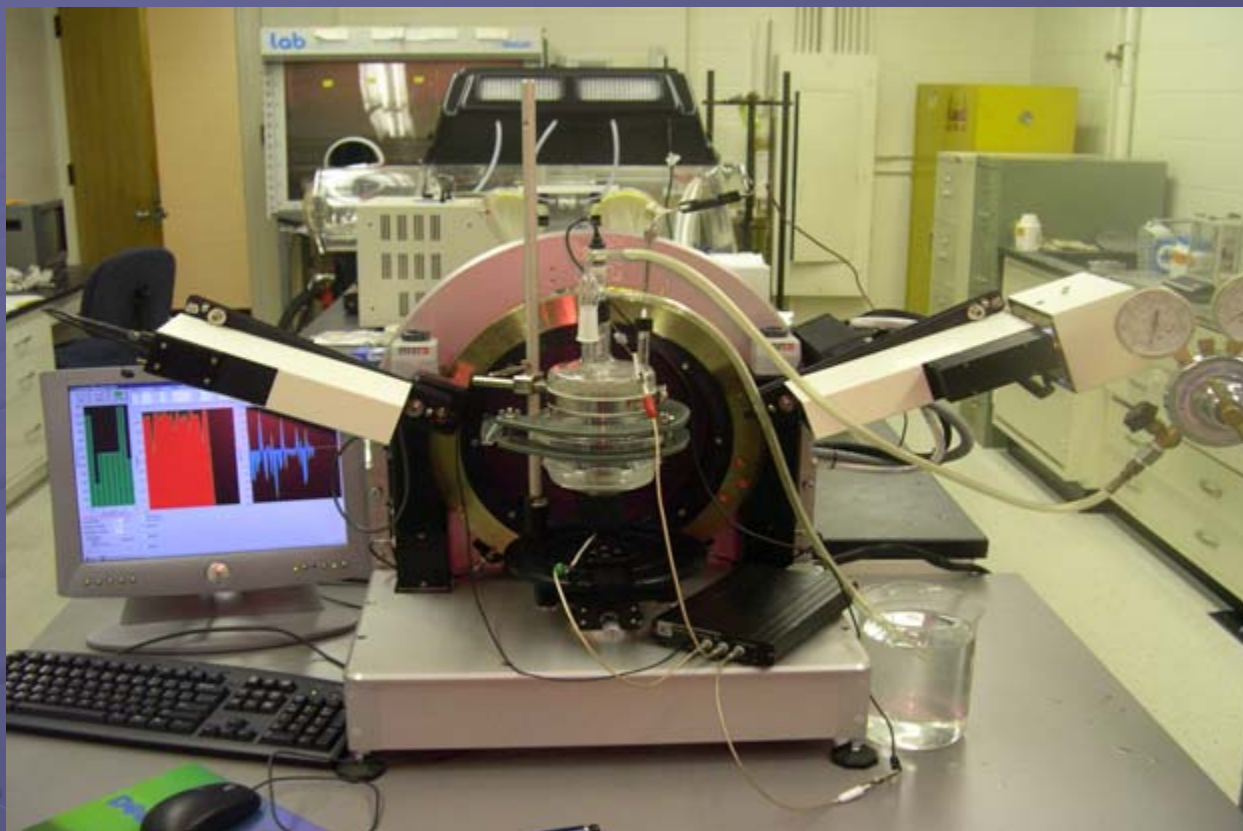
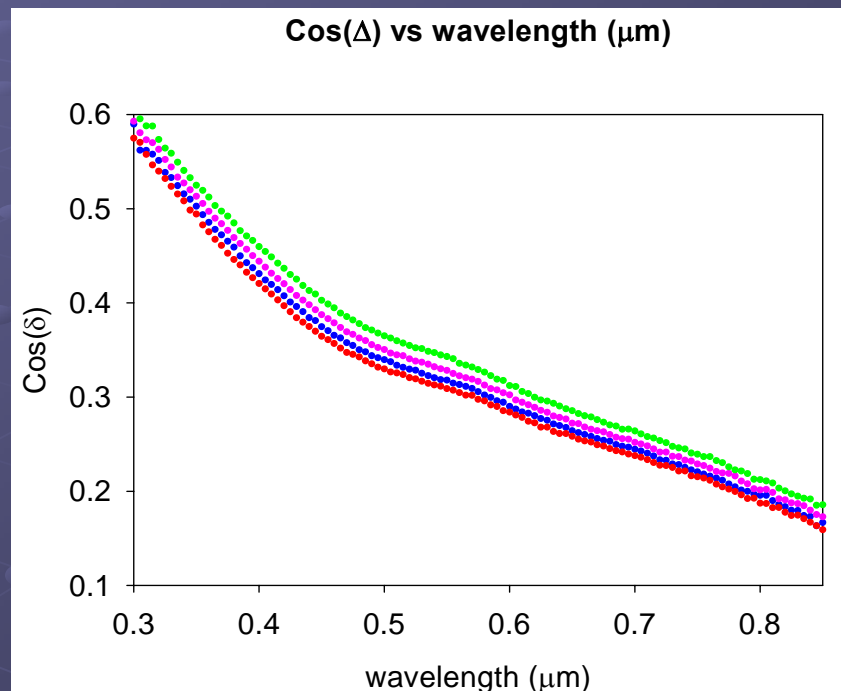
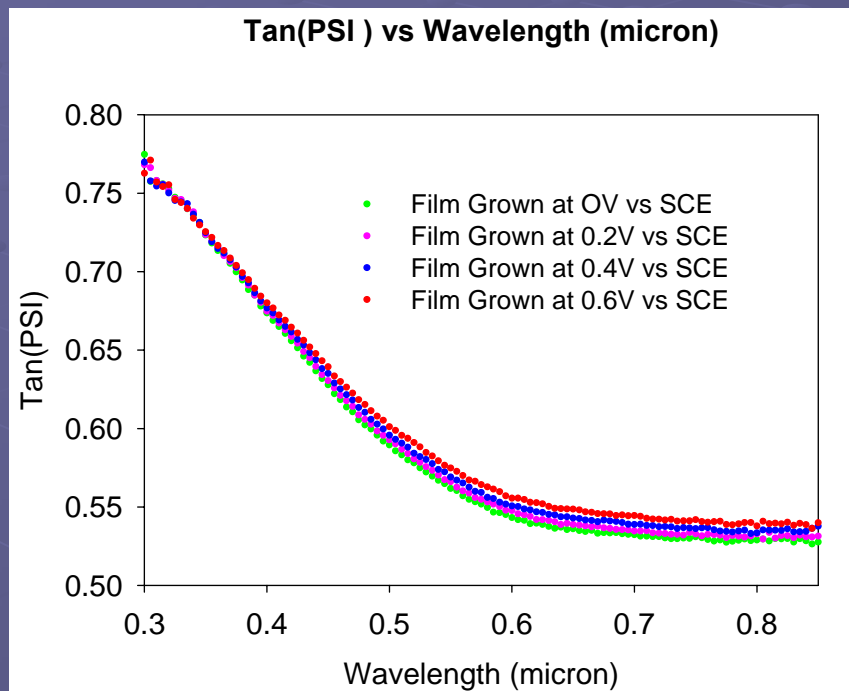


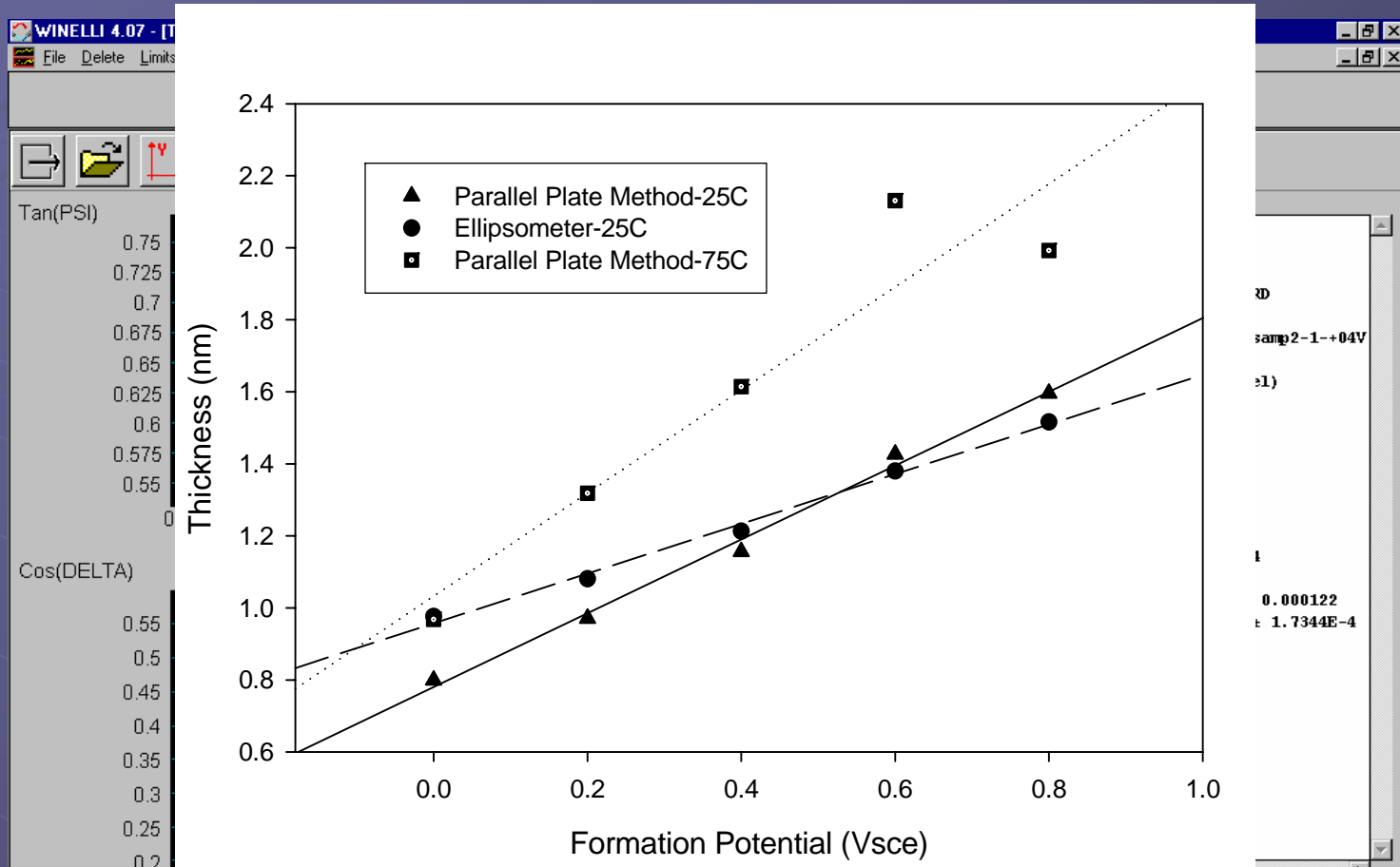
**Figure 1.** Picture of the spectroscopic ellipsometer and associated systems. The PC used to collect the ellipsometric and impedance data (a). Two arms of ellipsometer-used to detect the changes in reflected light (b). Potentiostat/Frequency Response Analyzer (FRA) for controlling the potential at the working electrode and measuring AC impedance (c) . The cell containing the electrochemical set-up (d) .

# Measuring Film Thickness at 25 C with Ellipsometry



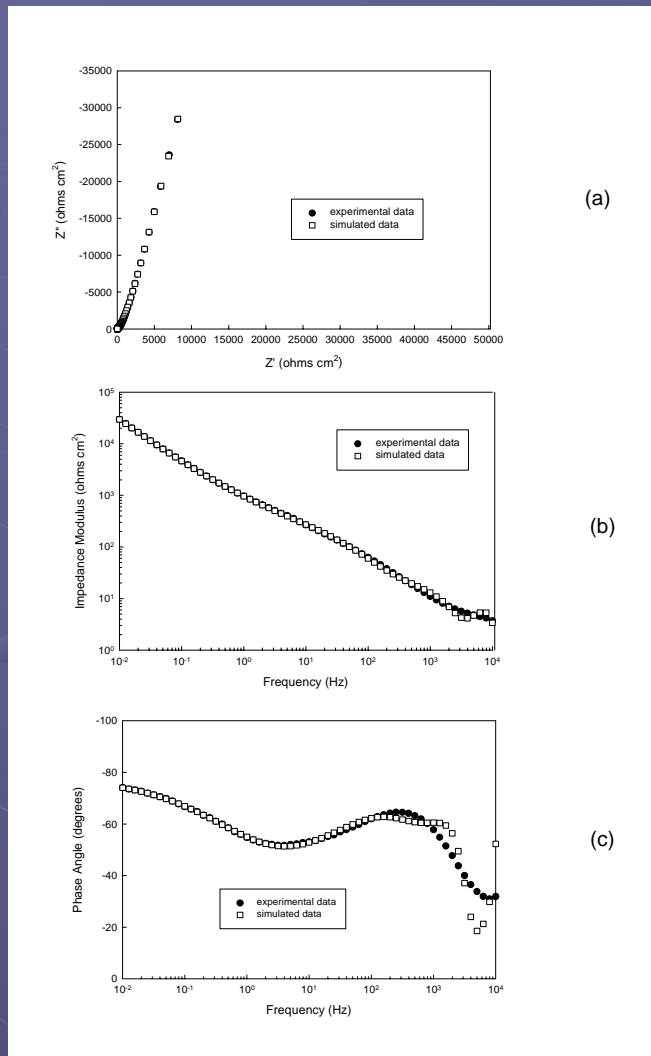
Ellipsometry results showing the increase in film thickness with potential in a boric acid solution at room temperature. EDTA was added to the solution to prevent the formation of the outer precipitation layer. Regression analysis was performed using the optical constants for iron and the film. The thickness was shown to increase from 7 Å to 1.6 nm. Transient measurements were also recorded for one wavelength (632 nm), but further analysis needs to be made.

# Ellipsometry Regression Results



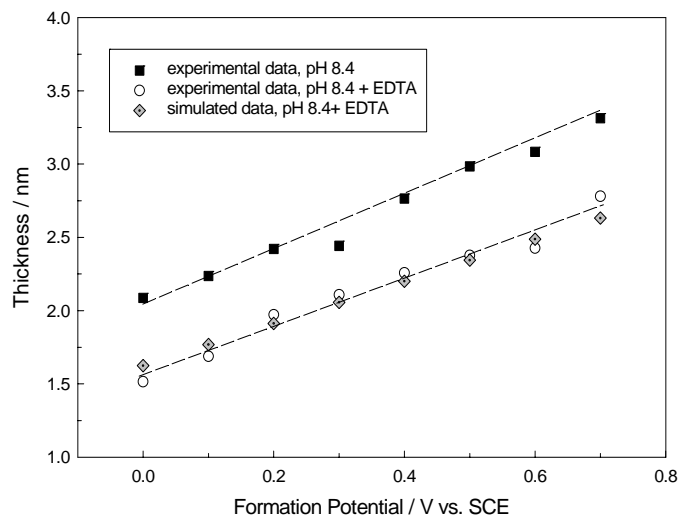
Iron Oxide thickness measurements for films grown at different potentials in borate buffer solutions containing EDTA. Ellipsometry measurements at 75° C contained too much noise; therefore the parallel plate capacitor method was employed. The parallel plate method is provided for comparison purposes at 25° C.

# Comparing Calculated Data to Experimental

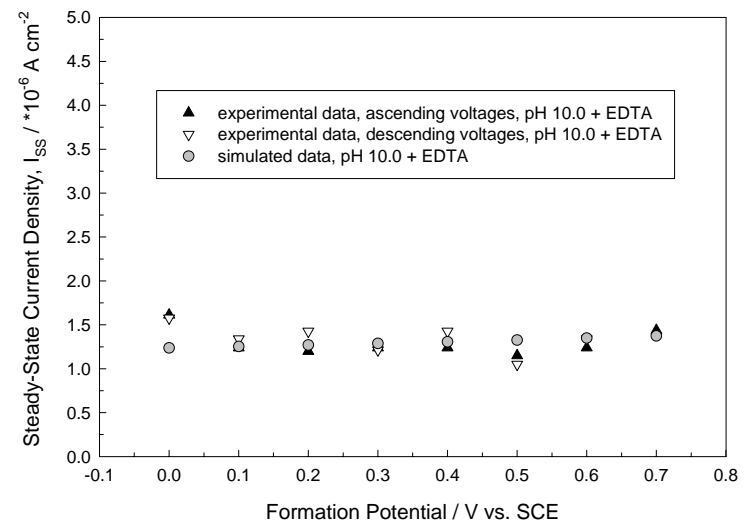


Nyquist plot (a) and Bode plots (b, c) of impedance data for the passive film formed on iron in borate buffer solution with 0.01 M EDTA (pH 8.15) at an applied film formation voltage of 0.2 V vs. SCE. Closed circles represent experimental data and open squares represent simulated data using nonlinear fitted parameters.

# Predicted vs. Experimental Data



Steady state film thickness for the passive film on iron. Simulated data were calculated using fundamental parameters in the Point Defect Model.

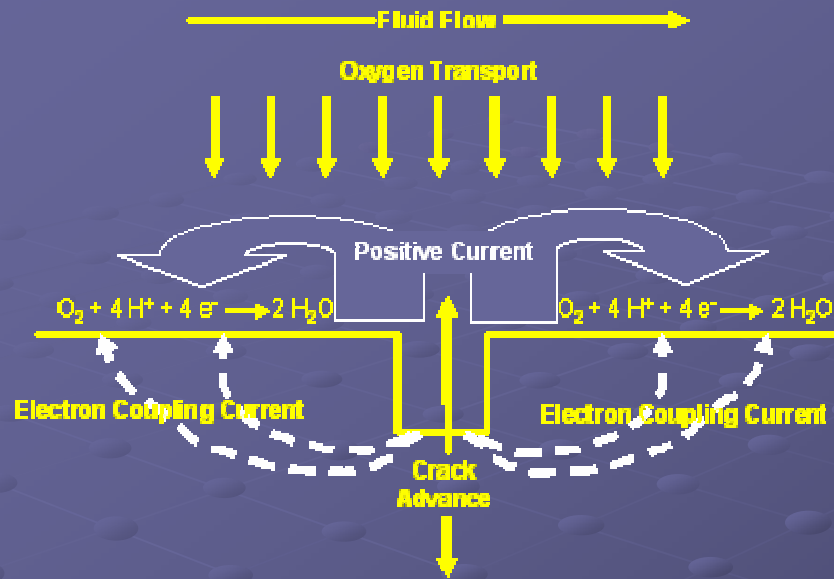


Steady state current for the passive film on iron. Simulated data were calculated using fundamental parameters in the Point Defect Model.

# Hydrogen Induced Fracture (HIF)

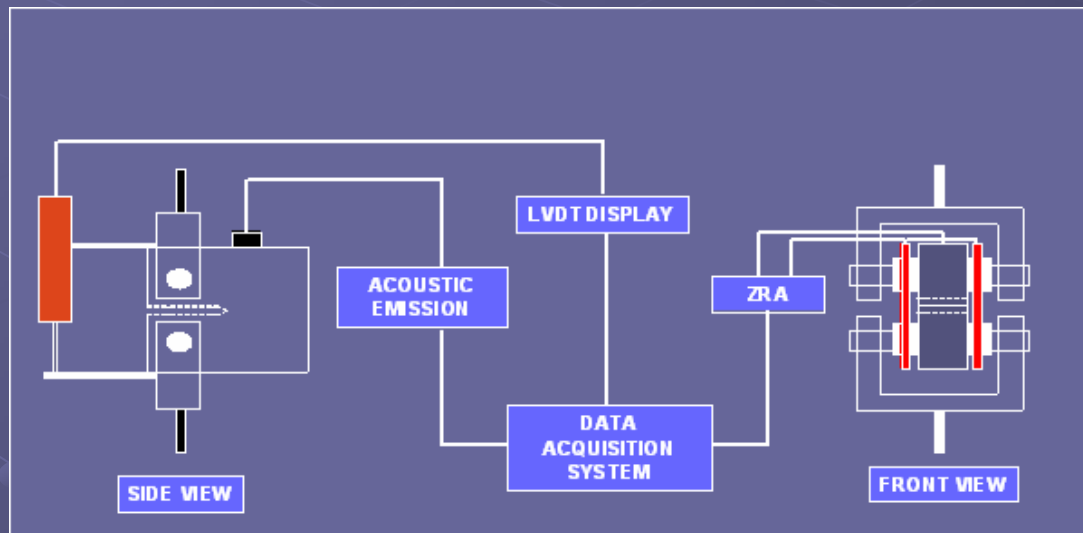
- HIF of weld Heat Affected Zones (HAZs) poses a significant threat to tank integrity.
- HAZs contain martensite, are hard, and are therefore susceptible to HIF.
- Previous work in this project, by monitoring the coupling current between the crack and the external surfaces, showed that the crack propagates via discrete events having super grain dimension.
- Data are consistent with HIF.
- Current work correlates the signatures of the discrete fracture events in the coupling current with acoustic emissions as a means of unequivocally confirming the origin of the transients in the current.

# Caustic cracking of AISI 4340 steel – Coupling of internal and external environments

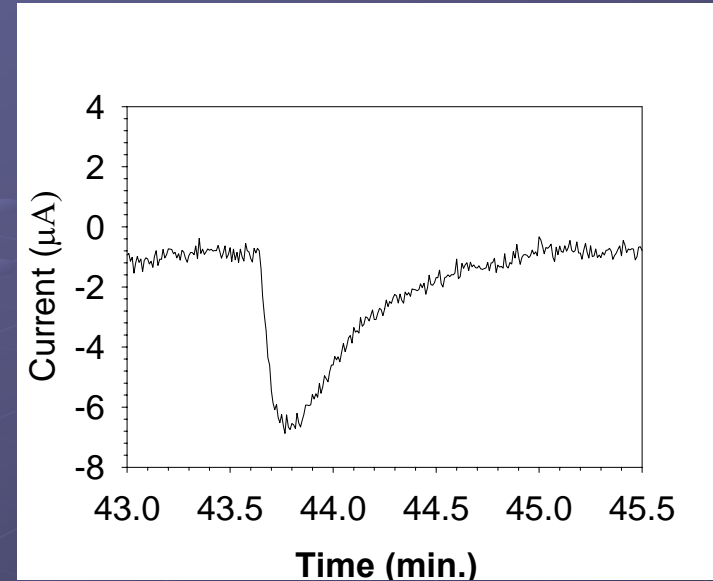
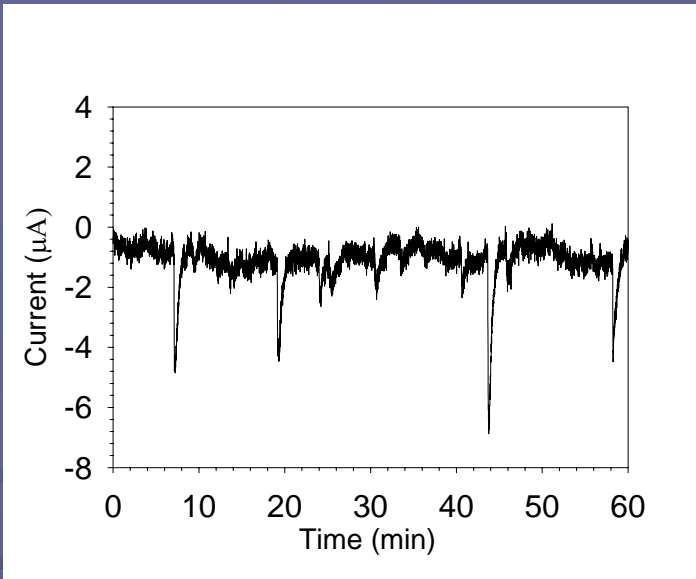


The coupling current is required by the differential aeration hypothesis for localized corrosion and the conservation of charge requires that this current be equal to the positive ionic current flowing through the solution from the crack to the external surface.

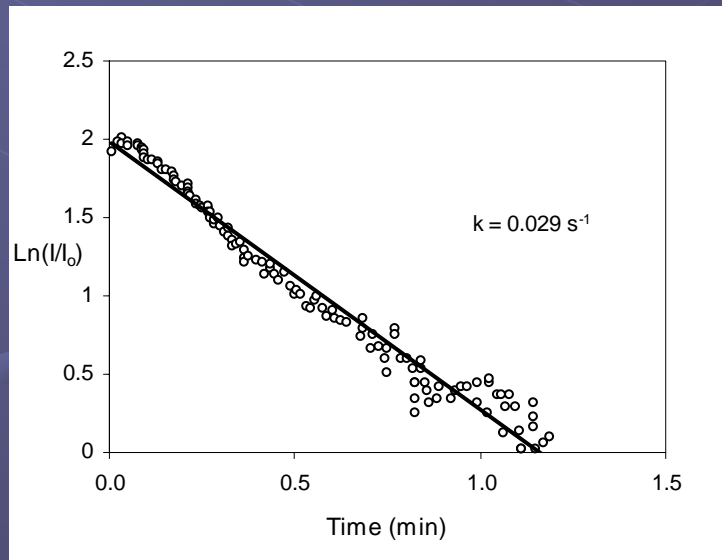
- Material – AISI 4340 steel
- Heat treated to simulate HAZ
- Environment - NaOH
- Cathodes – 1010, 1018, Pt
- The C (T) fracture mechanics specimen is coated with PTFE to inhibit the cathodic reduction of oxygen on the specimen surface.
- The electron current flows from the crack tip to the side cathodes via a zero resistance ammeter, which is used for its measurement
- LVDT and Acoustic emission Apparatus to simultaneously monitor the Crack opening displacement and acoustic activity respectively.



## Coupling current data from AISI 4340 steel in 6 M NaOH at 70 °C

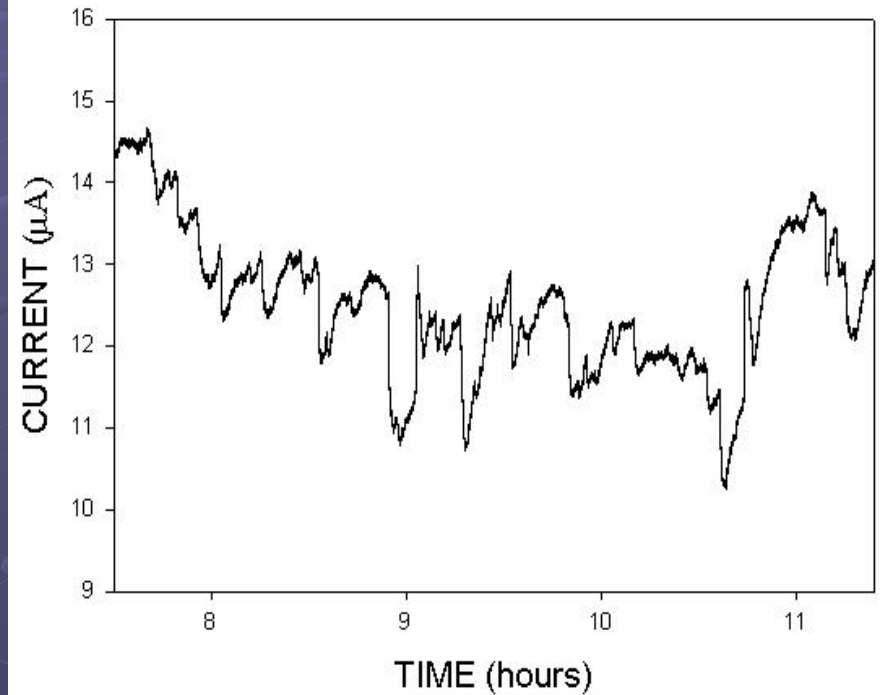
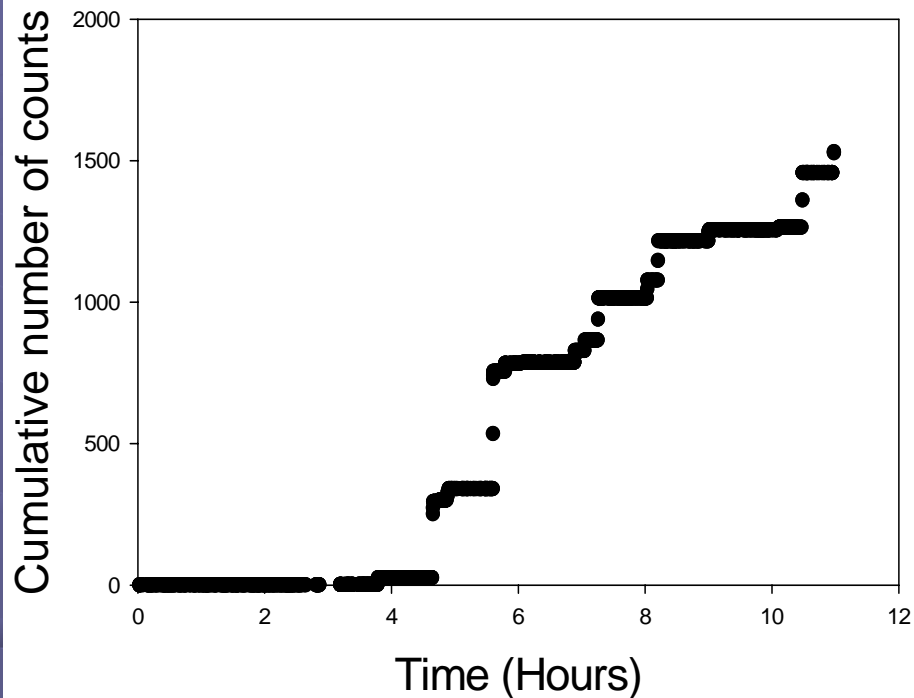


Typical transients in the (electron) coupling current from 5 to 52 hours after load application in AISI 4340 steel in 6M NaOH solution at 70 °C.



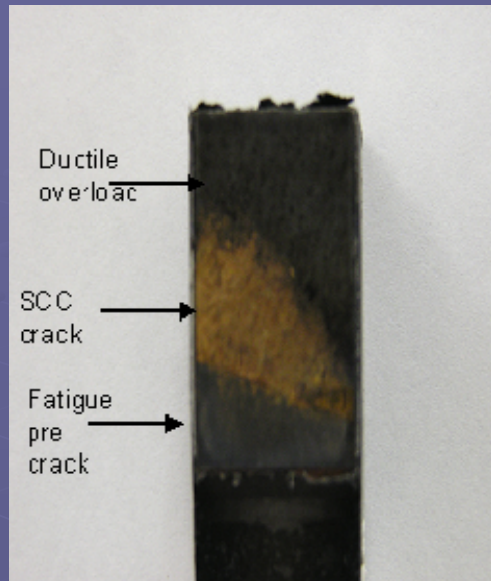
First order kinetic plot of the repassivation current shown in the previous figure

## Acoustic emission data from AISI 4340 steel in 6 M NaOH at 70 °C

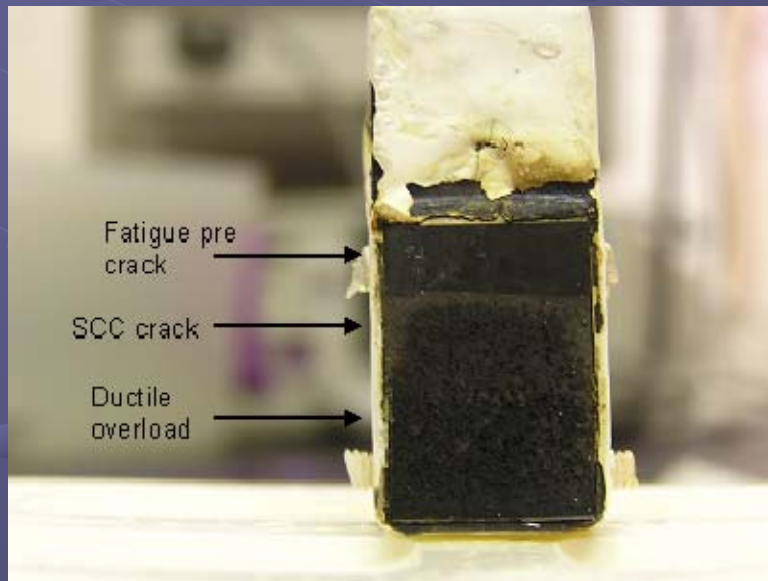


Cumulative acoustic emission counts vs. time after the application of load. The acoustic activity monitored over a period of 11 hours mostly coincides with the noise transients shown in the next figure, confirming the occurrence of microfracture events.

## Proof of existence of coupling in the system



One half of the fractured CT specimen with external cathode loaded only on one side (Left side). Notice that the crack has grown predominantly in the left hand side showing that a major portion of the cathodic reaction occurs on the external cathode. This is excellent evidence for coupling.



One half of the fractured CT specimen showing a concave crack front, which is a again a very good evidence for the existence of coupling in the system.

# Microfracture event dimension and mechanism of caustic cracking in AISI 4340 steel

$$\frac{dL}{dT} = \frac{2r^2 f}{B} \text{ (crack growth rate)}$$

$$r = \sqrt{\frac{B \frac{dL}{dt}}{2f}} \text{ (event dimension)}$$

For 6M NaOH

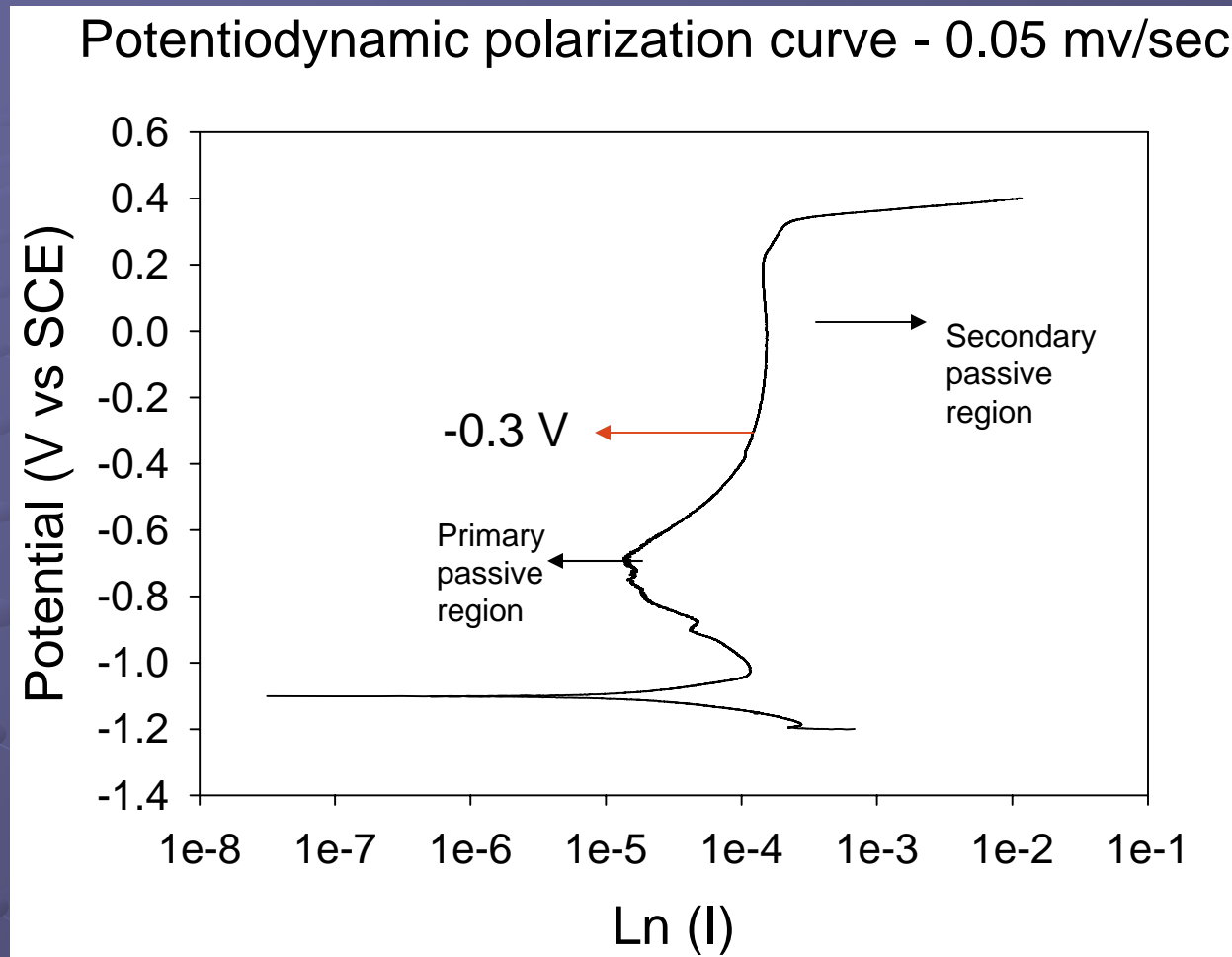
$$\begin{aligned} dL/dt &= 5.3 \times 10^{-8} \text{ cm/s} \\ B &= 2.7 \text{ cm} \\ f &= 0.003 \text{ s}^{-1} \end{aligned}$$

HYDROGEN EMBRITTLEMENT

$$r = 49 \mu\text{m}$$

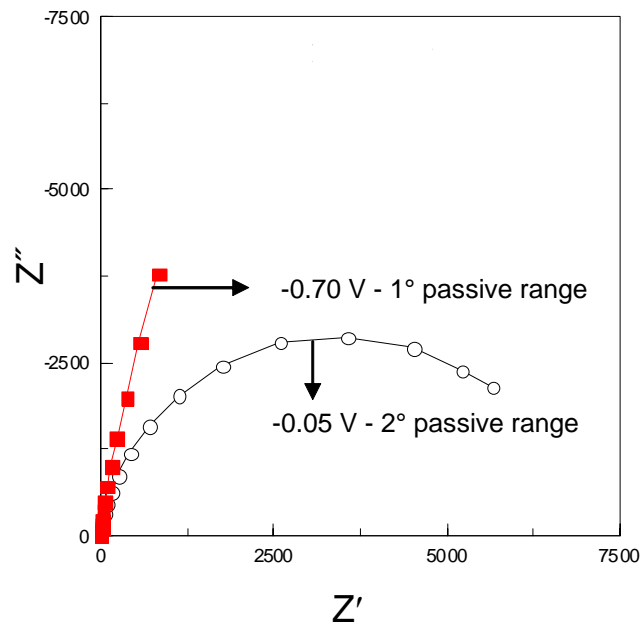
HOW ?

## Potentiodynamic polarization curve of AISI 4340 steel in NaOH solution

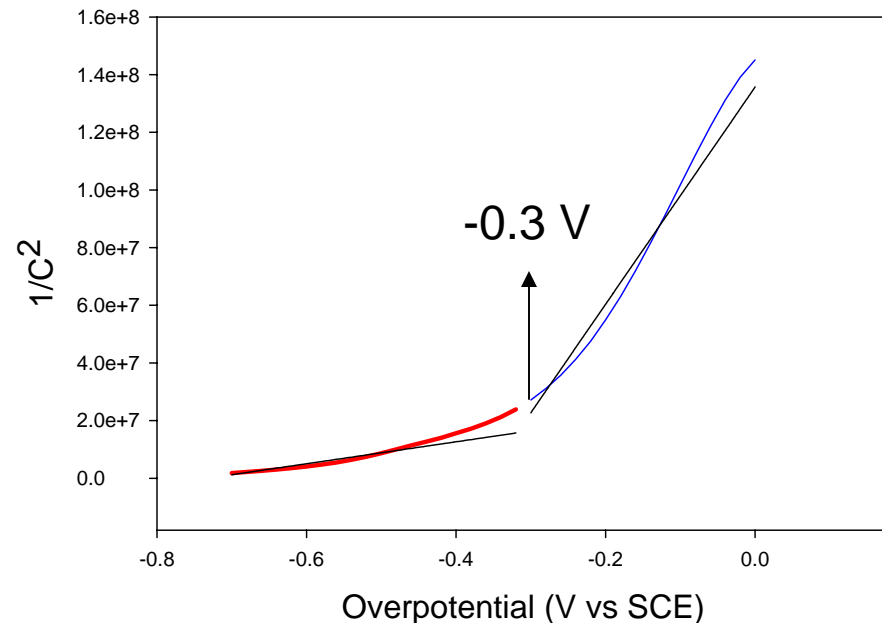


Potentiodynamic polarization curve of AISI 4340 steel in 8 M NaOH solution at 70 °C at a scan rate of 0.1 mV/sec. Notice the presence of two distinct passive regions that are characterized by oxide films of different chemical composition

# Impedance and Mott-Schottky plots of AISI 4340 steel in 8 M NaOH at 70 °C



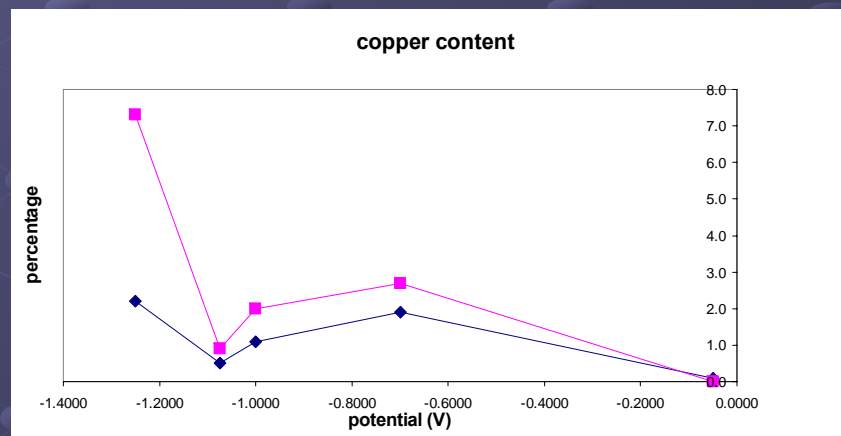
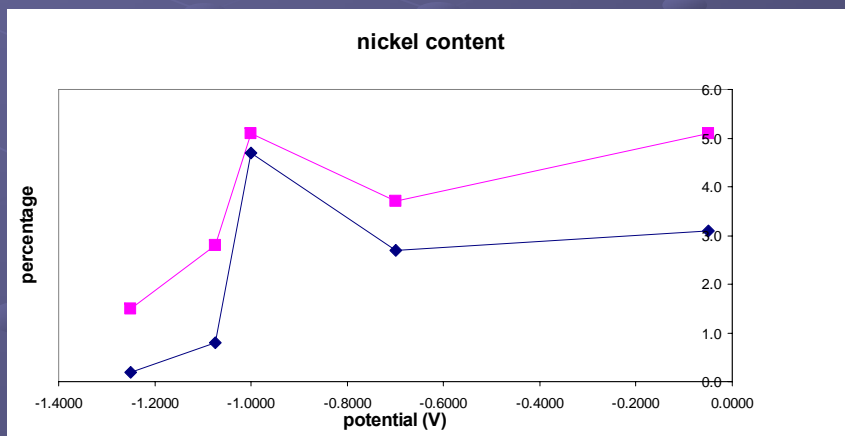
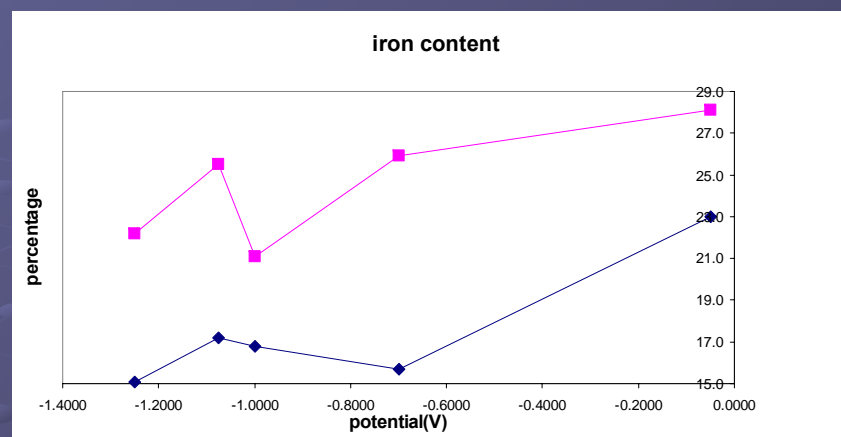
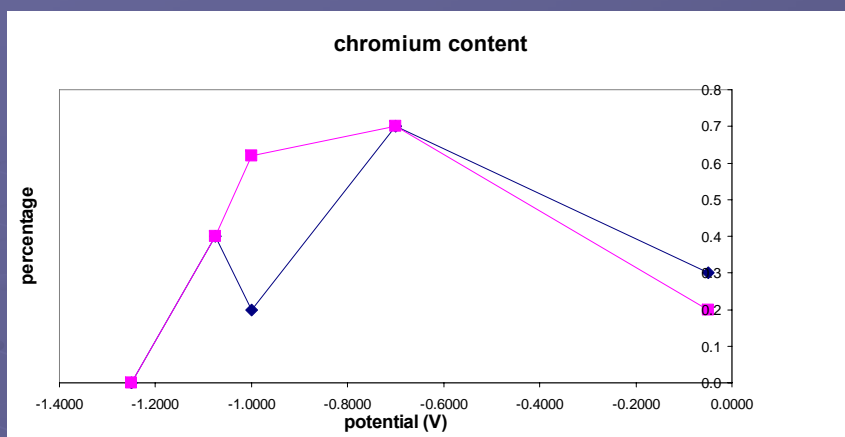
Mott-Schottky plot of AISI 4340 steel in 8M NaOH solution showing two regions of distinctly different slopes (defect concentration)



Impedance plot of AISI 4340 steel in 8 M NaOH at 70 °C shows that the oxide film formed in the primary passive region has a higher impedance in comparison to the secondary passive region.

Mott – Schottky plot of AISI 4340 steel in 8 M NaOH at 70 °C shows a sudden increase in the slope at the same potential range where the transition from primary to secondary passive range occurs

## XPS studies – Chemical composition of oxide film formed at different potentials



XPS data showing the formation of an oxide film with a low percentage of chromium and copper and a high percentage of iron in the secondary passive region (-0.05 V vs SCE). The vice versa is seen in the oxide film formed in the primary passive region (-0.70 V vs SCE).

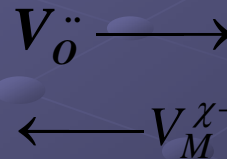
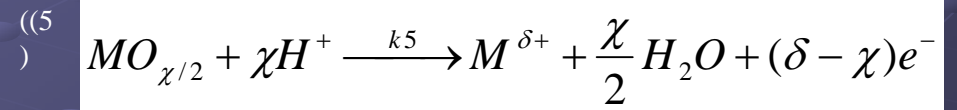
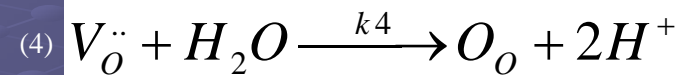
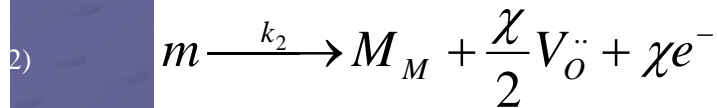
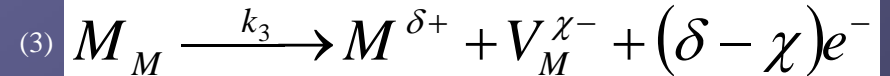
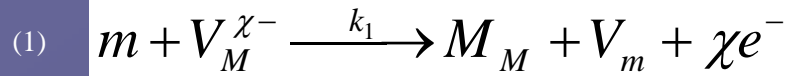
# Chloride-Induced Passivity Breakdown

- Specific ions induce localized breakdown of the passive films on metals. Chloride ion ( $\text{Cl}^-$ ) is the most deleterious species towards iron and is present in the liquid waste.
- The Point Defect Model postulates that  $\text{Cl}^-$  absorbs into oxygen vacancies at the barrier oxide/solution interface, thereby causing cation vacancies to condense at the metal/film interface and ultimately to breakdown of the film.
- Is this mechanism correct?
- Unfortunately, we cannot “see” cation vacancies in the passive film on iron (via Mott-Schottky analysis), because the film is n-type (due to the dominant defect being the oxygen vacancy or the cation interstitial), rather than being p-type due to an excess of cation vacancies.
- However, the passive film on nickel is p-type, demonstrating that the dominant defect is the cation vacancy, so that any change in cation vacancy concentration induced by  $\text{Cl}^-$  is readily ascertained using M-S analysis.
- Chromium and aluminum also form p-type passive films and hence are candidate systems for this type of analysis.
- Most, if not all metals, exhibit the same relationships between dependent and independent breakdown parameters and hence it appears that a common mechanism operates in all systems.

Metal

Passive Film

Solution



$x = L$

$x = 0$

**Figure 1:** Schematic of physico-chemical processes that occur within a passive film according to the Point Defect Model.  $m$  = metal atom,  $V_M^{\chi-}$  = metal vacancy,  $M_M$  = cation in cation site,  $V_{O^{\cdot\cdot}}$  = oxygen vacancy,  $M^{\delta+}$  = cation in solution,  $O_O$  = oxygen ion in anion site,  $MO_{\chi/2}$  = stoichiometric passive film. Metal vacancies are produced at the film/solution interface, but are consumed at the metal/film interface. Likewise, oxygen vacancies are formed at the metal/film interface, but are consumed at the film/solution interface. Consequently, the fluxes of metal vacancy and oxygen vacancy are in the directions indicated.

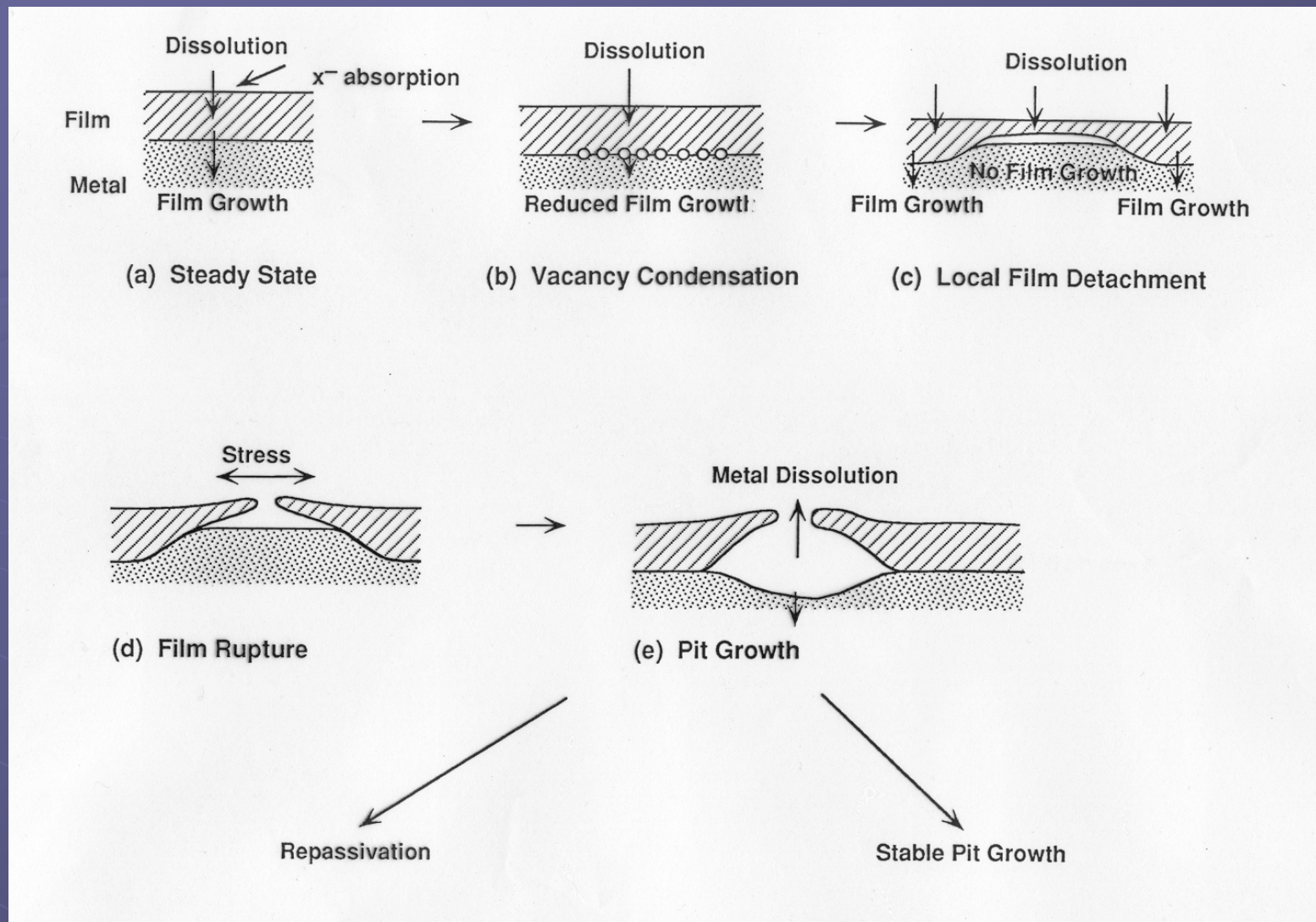


**Figure 2:** Cartoon outlining various stages of pit nucleation according to the Point Defect Model.

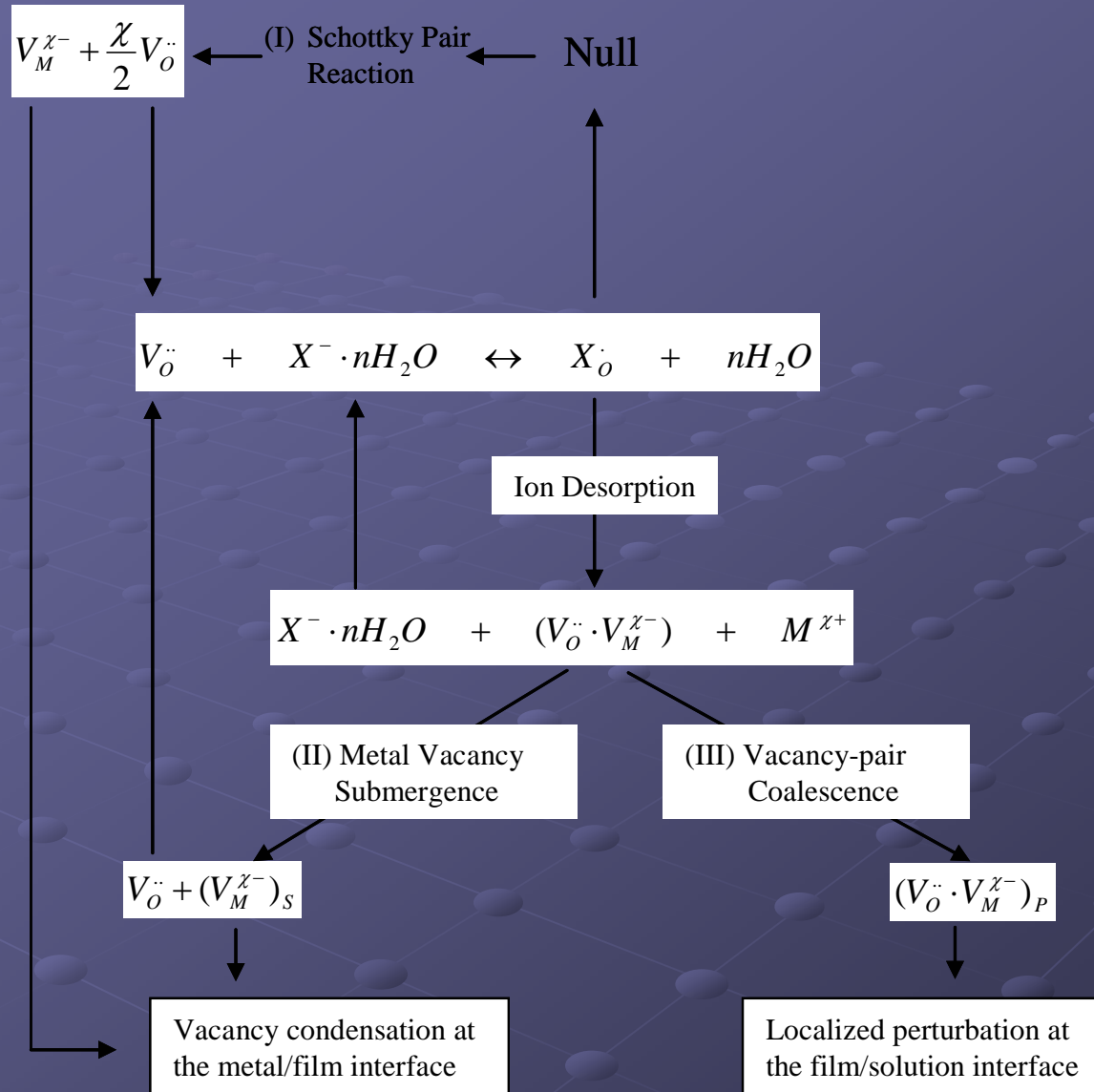


**Figure 3:** Postulated reactions for cation vacancy generation at the barrier layer/solution interface according to the Point Defect Model.

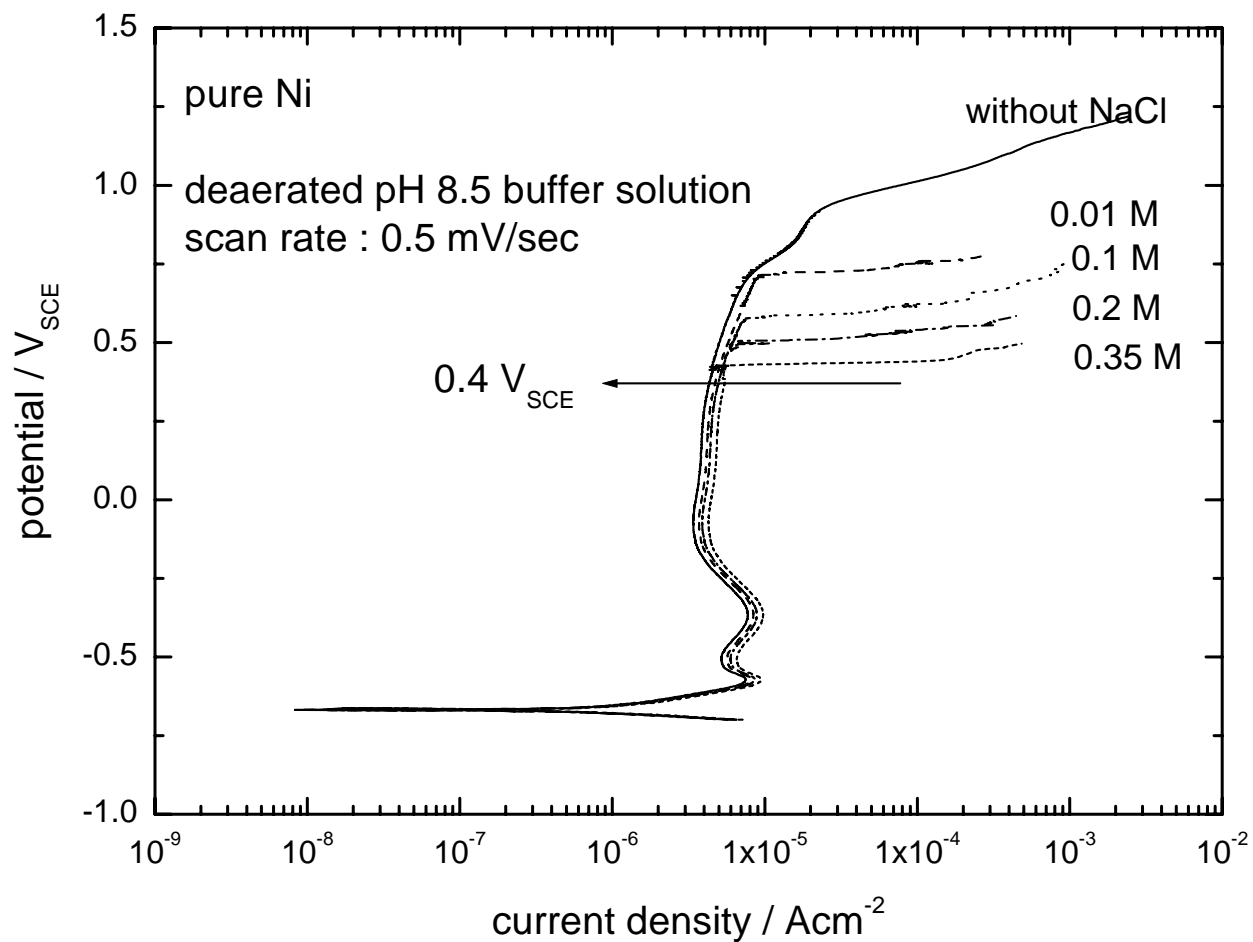


**Figure 7:** Polarization curves of Ni in deaerated pH 8.5 buffer solution at ambient temperature with different Cl<sup>-</sup> concentration.

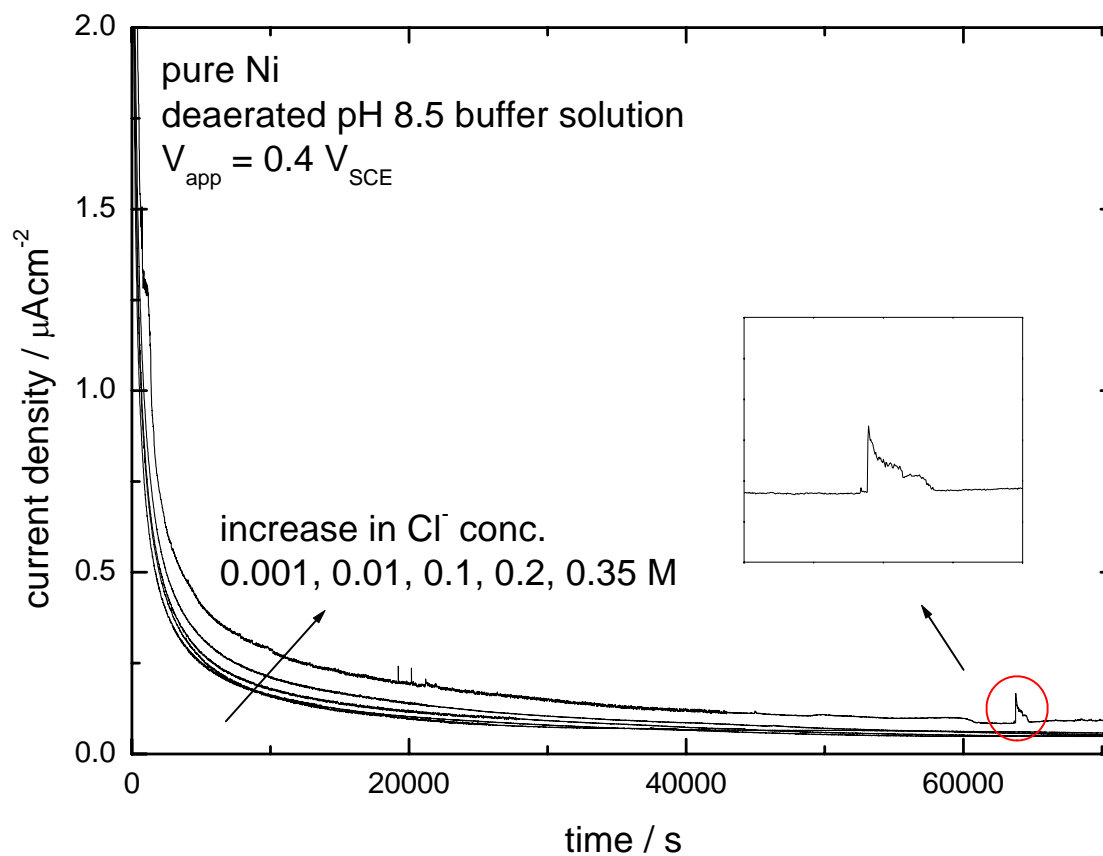


**Figure 8:** Current transient curves of Ni measured at 0.4 VSCE in deaerated pH 8.5 buffer solutions containing different concentration of NaCl at ambient temperature. The concentration of  $Cl^-$  was controlled from 0 to 0.35 M by adding NaCl to the solution.

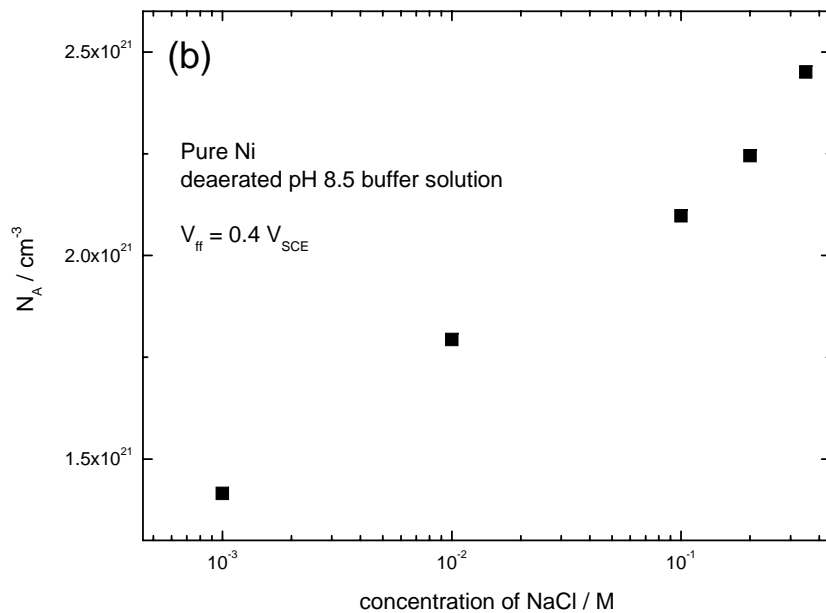
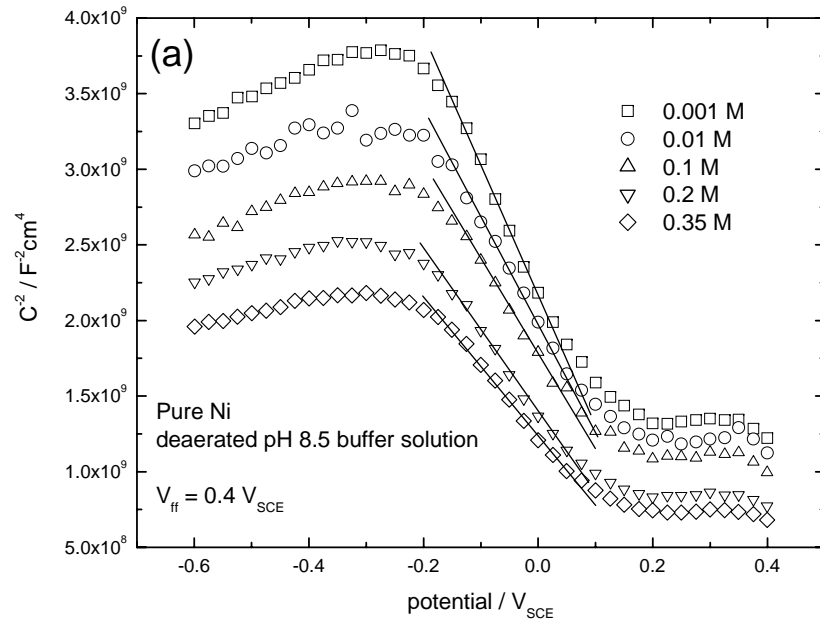


**Figure 9:**

(a) Mott-Schottky plots for the passive film formed on Ni in deaerated pH 8.5 buffer solution with different concentration of Cl<sup>-</sup> at 0.4  $V_{SCE}$  for 24 h at ambient temperature. Mott-Schottky plots were measured at a frequency of 1 kHz.

(b) Acceptor density in the passive film on Ni calculated from the linear slope of Fig. 9(a).

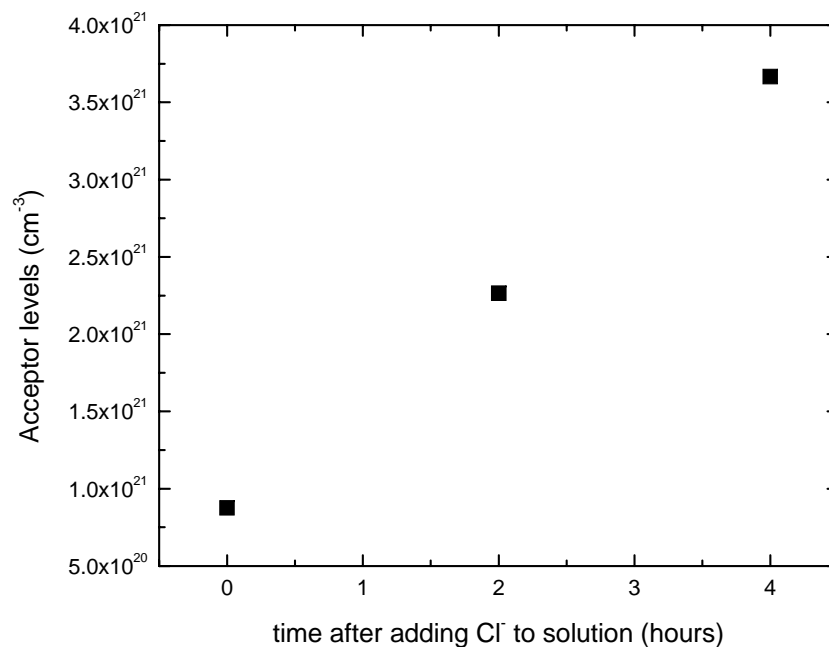
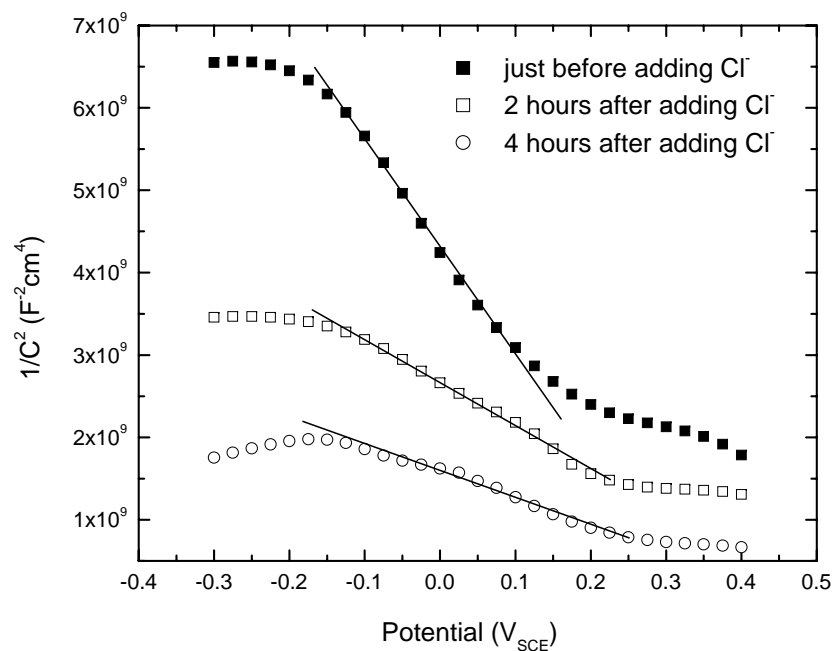


**Figure 10:** (a) Mott-Schottky plots for the passive film formed on Ni in deaerated, pH 8.5 borate buffer solution at  $0.4 V_{SCE}$ , calculated from capacitance data measured at a frequency of 1 kHz, as a function of the time after which chloride ion (0.1 M) was added to the solution. (b) Acceptor concentration as a function of time after the addition of chloride ion.

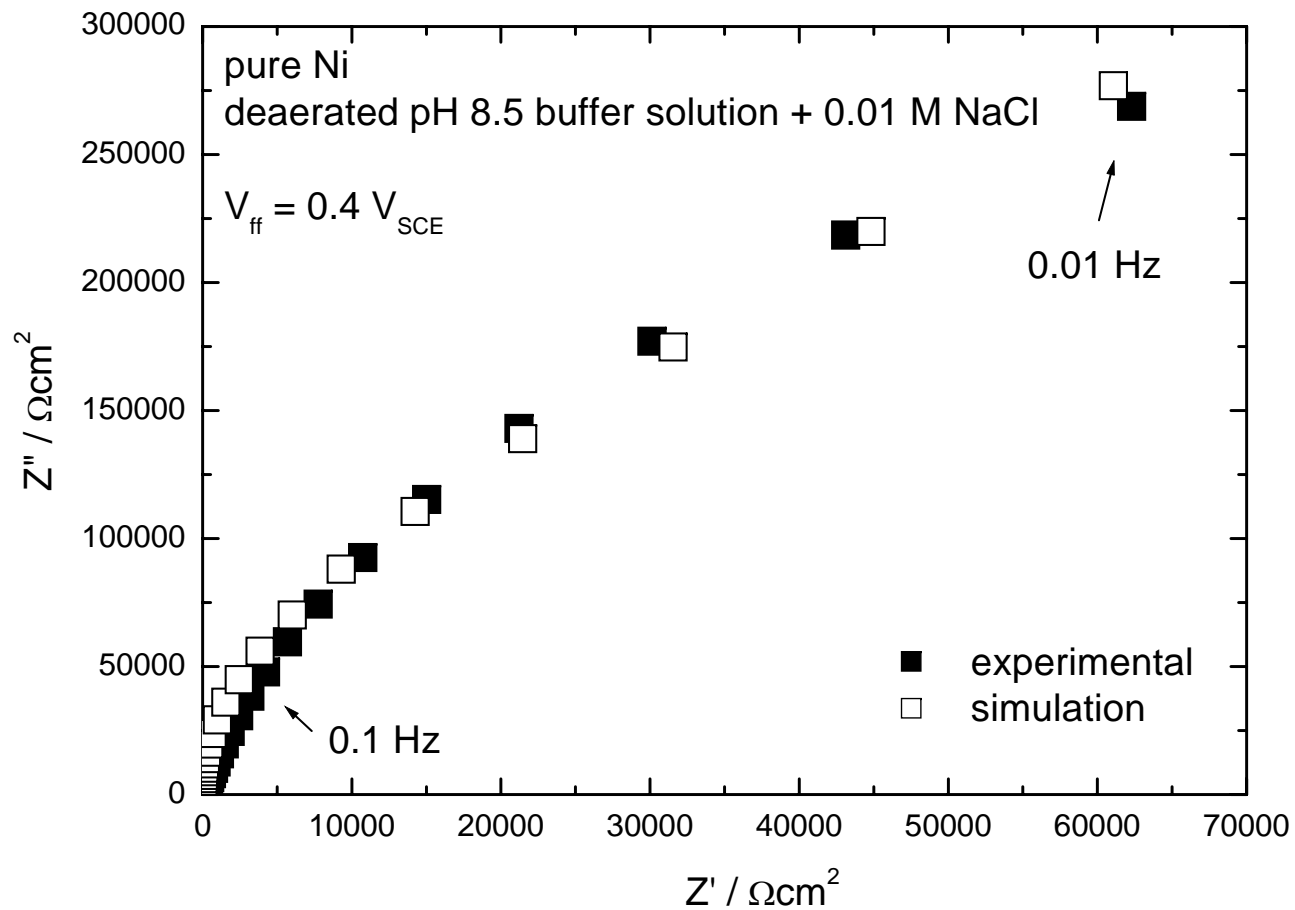


**Figure 10:** Nyquist plots for the passive film on Ni in Cl<sup>-</sup> containing, deaerated pH 8.5 buffer solution at  $0.7 V_{SCE}$ , together with the model fit by the PDM.

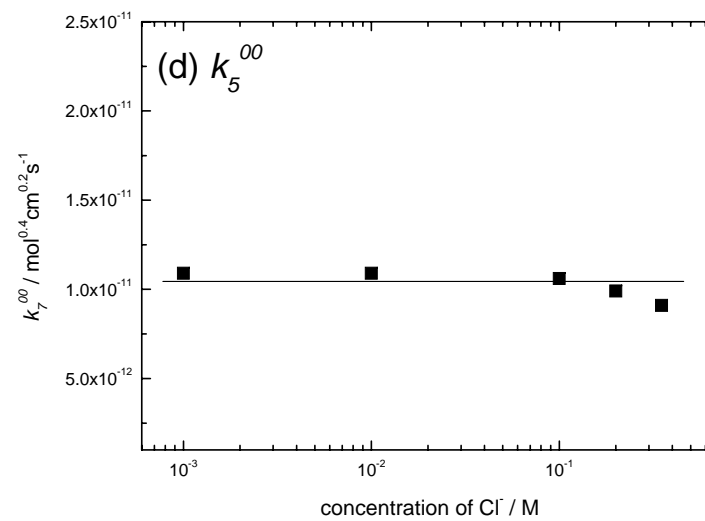
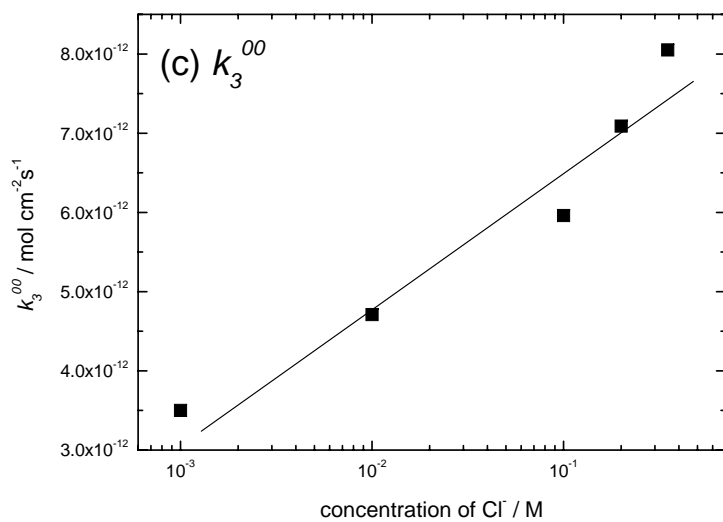
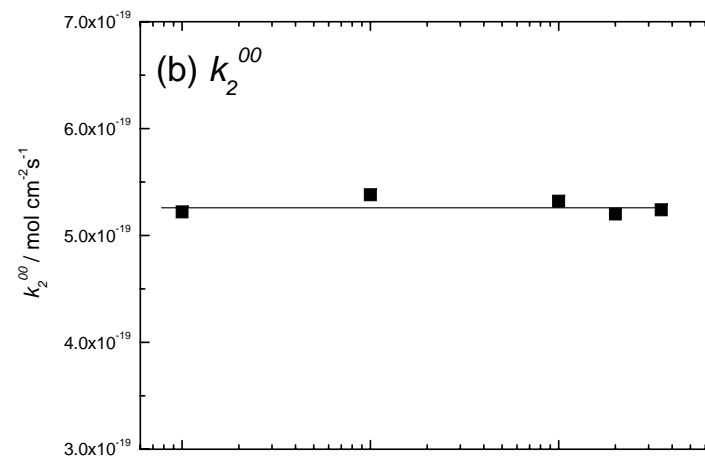
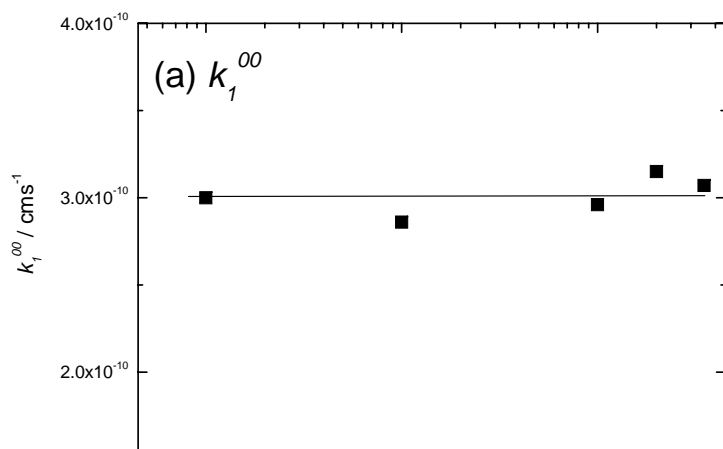
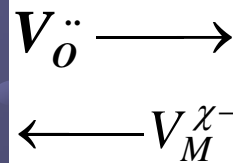
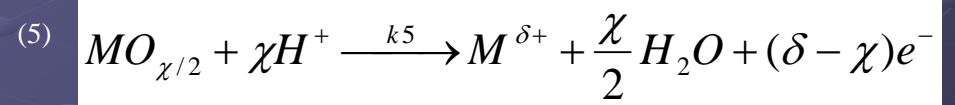
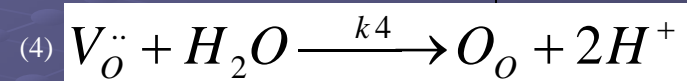
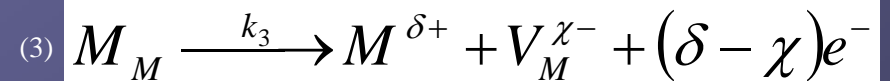
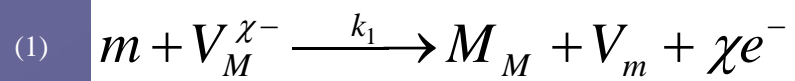


**Figure 11:** Effect of  $[\text{Cl}^-]$  on  $k_i^{00}$  for nickel in chloride solution. The standard rate constants were determined by optimization of the PDM on the experimental impedance data.

Metal

Passive Film

Solution



$x = L$

$x = 0$

**Figure 1:** Schematic of physico-chemical processes that occur within a passive film according to the Point Defect Model.  $m$  = metal atom,  $V_M^{\chi-}$  = metal vacancy,  $M_M$  = cation in cation site,  $V_O^{\cdot\cdot}$  = oxygen vacancy,  $M^{\delta+}$  = cation in solution,  $O_O$  = oxygen ion in anion site,  $MO_{\chi/2}$  = stoichiometric passive film. Metal vacancies are produced at the film/solution interface, but are consumed at the metal/film interface. Likewise, oxygen vacancies are formed at the metal/film interface, but are consumed at the film/solution interface. Consequently, the fluxes of metal vacancy and oxygen vacancy are in the directions indicated.

# Major Accomplishments (2004)

- Demonstrated that Wavelet Analysis (WA) of Electrochemical Emission Spectroscopic (electrochemical noise) data is capable of not only characterizing the severity of corrosion, but is also able to differentiate between general corrosion and pitting on carbon steel in simulated Liquid Waste environments.
- Further characterized the passive state on iron in borate buffer and hydroxide environments and develop methods for extracting values for key parameters in the Point Defect Model. Used ellipsometry to obtain the thickness of the passive film on iron as a function of voltage.
- Demonstrated that the fracture of simulated Heat Affected Zones (HAZs) in carbon steel in simulated Liquid Waste is a Hydrogen Induced Fracture phenomenon. Cracks propagate in discrete steps and the resulting transients in the coupling current correlate with acoustic emission signals with good fidelity.
- Demonstrated two distinct regions in the passive state for iron in concentrated hydroxide solution, as indicated by Mott-Schottky analysis. The low potential region is characterized by a much higher donor concentration than is the high potential region, possibly corresponding to a transition in the barrier layer from  $\text{Fe}_3\text{O}_4$  (magnetite) to  $\gamma\text{-Fe}_2\text{O}_3$  (maghemite) at a potential of ca.  $-0.30 \text{ V}_{\text{SCE}}$ .
- Unequivocally demonstrated that the role of  $\text{Cl}^-$  in the breakdown of passivity in nickel is the enhanced generation of cation vacancies at the film/solution interface as postulated by the Point Defect Model.
- Involved graduate and undergraduate students from four nations (India, Republic of China, South Korea, and Spain) in our research, with their stays being mostly supported by their home governments.